TU Delft

Delft University of Technology

# Assembly of semi-analytical models to address linear buckling and vibration of stiffened composite panels with debonding defect

Castro, Saullo G.P.; Donadon, Maurício V.

**DOI**
10.1016/j.compstruct.2016.10.026

**Publication date**
2017

**Document Version**
Final published version

**Published in**
Composite Structures

**Citation (APA)**
Castro, S. G. P., & Donadon, M. V. (2017). Assembly of semi-analytical models to address linear buckling and vibration of stiffened composite panels with debonding defect. *Composite Structures*, *160*, 232-247. https://doi.org/10.1016/j.compstruct.2016.10.026

**Important note**
To cite this publication, please use the final published version (if applicable).
Please check the document version above.

**Copyright**
Other than for strictly personal use, it is not permitted to download, forward or distribute the text or part of it, without the consent of the author(s) and/or copyright holder(s), unless the work is under an open content license such as Creative Commons.

**Takedown policy**
Please contact us and provide details if you believe this document breaches copyrights.
We will remove access to the work immediately and investigate your claim.

*This work is downloaded from Delft University of Technology.*
*For technical reasons the number of authors shown on this cover page is limited to a maximum of 10.*

Composite Structures 160 (2017) 232–247

Contents lists available at ScienceDirect

Composite Structures

journal homepage: www.elsevier.com/locate/compstruct

# Assembly of semi-analytical models to address linear buckling and vibration of stiffened composite panels with debonding defect

Saullo G.P. Castro [a,*], Maurício V. Donadon [b]

[a] Embraer, Brazilian Aerospace Company, 12227-901 São José dos Campos, SP, Brazil
[b] ITA, Technological Institute of Aeronautics, Department of Aeronautical Engineering, São José dos Campos, SP, Brazil

ARTICLE INFO

*Article history:*
Received 23 June 2016
Revised 10 October 2016
Accepted 11 October 2016
Available online 15 October 2016

*Keywords:*
Composite
Defect
Linear buckling
Vibration
Semi-analytical
Stiffened plate
Stiffened shell

ABSTRACT

The substitution of conventional mechanical fasteners by adhesive joints has been advocated by the aircraft and aerospace industries due to the weight saving potential. Flaws such as debonding of the adhesive layer between the skin and the stiffener may greatly affect the structural behavior of composite panels. Within this context, this work presents a semi-analytical approach for the numerical investigation on the effects of skin-stiffener bonding flaw size on the vibration and linear buckling behavior of T-stiffened composite panels. Skin and stiffener have been modeled using an assembly of curved and flat panel components, with each domain approximated using a set of hierarchical polynomial functions. A penalty-based approach has been used to assemble the various domains and to model the debonded region between the stiffener flange base and the plate. This approach ensures full compatibility in terms of displacements and rotations between the stiffener's base top face and the panel bottom face allowing to model different skin/stiffener debonding lengths. The results obtained using the proposed semi-analytical models have been compared and verified against numerical predictions based on finite element analyses.

© 2016 Elsevier Ltd. All rights reserved.

## 1. Introduction

Flat and curved composite panels constitute a major portion of aircraft structures. They are found in aerospace structures such as wing surfaces, horizontal and vertical stabilizers, and fuselage sections as well as in spacecraft and missile structural applications [1]. Nowadays there exist many methods for bringing together stiffeners and skin in terms of the joining technique. Conventional mechanical joints such as bolted, pinned or riveted are preferred due to their simplicity and disassembly capability for both metallic or composite parts. However, mechanical joints are prone to local damage at the fastener holes due to stress concentrations [2–4], leading to the degradation of the joint which ultimately jeopardizes the structural integrity of the assembled structure. The demands for designing lightweight structures without any loss of stiffness and strength have turned many researchers and design engineers to seek for alternate joining methods. Adhesive bonding is a material joining process in which an adhesive placed between the adherent surfaces solidifies to produce an adhesive bond. The field of structural adhesive bonding has matured with the development of a wide range of adhesives from the chemical industry. Both adhesive bonding or co-cure offer several advantages over conventional joining technologies which includes [5]: (a) Often, thinner gage materials can be used with attendant weight and cost savings; (b) The number of production parts can be reduced, whereas the design is more simplified; (c) The need for milling, machining and forming operation of details is reduced; (d) Large area bonds can be made with a minimum work force without special skills; (e) Adhesive bonding provides a high strength to weight ratio with three times higher the shearing force of riveted joints; (f) Improved aerodynamic/hydrodynamic smoothness and visual appearance; (g) Use as a seal, and/or corrosion preventer when joining incompatible materials.

Most of the work reported in the open literature have focused on the effects of the skin-stiffener interfacial debonding flaws on the static behavior of stiffened composite panels. Previous studies on the effects of the skin/stiffened delamination in co-cured stiffened panels uniaxially loaded in compression in the post-buckling regime are presented in Refs. [6–9]. Ambur et al. [9] presented a similar study for composite panels loaded in shear. Rijn and Wiggenraad [10] investigated experimentally the strength of the skin-stiffener interface in composite aircraft panels using the seven-point bending test apparatus. Closed-form [11–14] and

* Corresponding author.
*E-mail address:* castrosaullo@gmail.com (S.G.P. Castro).

http://dx.doi.org/10.1016/j.compstruct.2016.10.026
0263-8223/© 2016 Elsevier Ltd. All rights reserved.

semi-analytical approaches [15–17] to deal with the local buckling of stiffened panels and plates have been presented in the literature, but a semi-analytical approach that takes into account global buckling modes and debonding flaws are currently not available.

The skin/stiffener interface behavior plays an important role in the overall dynamic characteristics of the stiffened panel, such as natural frequencies, mode shapes, and non-linear response characteristics to external excitations. The joint represents a discontinuity in the structure and results in high stresses that often nucleate failure [18]. The stresses and slip in the vicinity of contact regions determine the static strength, cyclic plasticity, frictional damping, and vibration levels associated with the structure. The need for developing methodologies for constructing predictive models of structures with joints and interfaces has recently been discussed by Dohner [19].

Modern mechanical design and analyses are based on deterministic finite element (FE) and multi-body dynamics computer codes [20]. The main objectives of these codes are to estimate the system eigenvalues, system response statistics, and probability of failure [21,22]. Ibrahim and Pettit [22] presented an assessment of the role of joint uncertainties and relaxation in the design and dynamic behavior of structural systems. Basic considerations in the design of joints of composite structures are discussed by Agarwal and Broutman [23].

The main goal of this paper is to present a semi-analytical approach to investigate the effects of skin-stiffener bonding flaw size on the linear buckling and vibration behavior of T-stiffened composite panels subjected to any static loads. Various laminate configurations for the skin and stiffener as well as different geometric configurations were investigated in an attempt to map the general behavior of such panels under the presence of a skin/stiffener debonding flaw. The problem is solved using an assembly of semi-analytical models that can be adapted to a large variety of problems, producing efficient parameterized tools for the investigation of various types of structures. The Ritz Method is chosen to derive the equations for each semi-analytical domain using the weak form, with each semi-analytical domain and their assembly formulated using the kinematic assumptions from the Classical Laminated Plate Theory (CLPT). Finite element models were used to verify the obtained results and the convergence behavior of the approximation functions here adopted.

## 2. T-Stiffened panel with debonded region

Fig. 1. shows a T-Stiffened panel with the respective coordinate system for the skin $(x,y,z)$, stiffener's base $(x',y',z')$ and flange $(x'',y'',z'')$. A debonding defect exists and it is assumed to always extend all over the stiffener's base width $(b_b)$ and has its length $\delta$ measured by its extent along coordinate $x$. The T-Stiffener is assumed to extend all over the skin panel length, parallel to $x$, with the origin of coordinate system $x'',y'',z''$ located at $y = b/2$. All dimensions necessary to define the T-Stiffener cross section and the skin thickness are also shown in Fig. 1.

In order to compute linear static displacements, linear buckling modes and vibration modes for the stiffened panel of Fig. 1, the authors have first attempted to apply a semi-analytical model for which the skin region was modeled using a single domain, with just one set of continuous approximation functions. For those attempts Legendre's hierarchical polynomials of orders as high as 24 for each coordinate were used as approximation functions for the displacements $u,v,w$, leading to an insufficient resolution of the displacement field. The successful strategy herein explained in details consists on dividing the skin, stiffener's base and stiffener's flange in subdomains, as illustrated in Fig. 2, where each subdomain has its own set of approximation functions and the

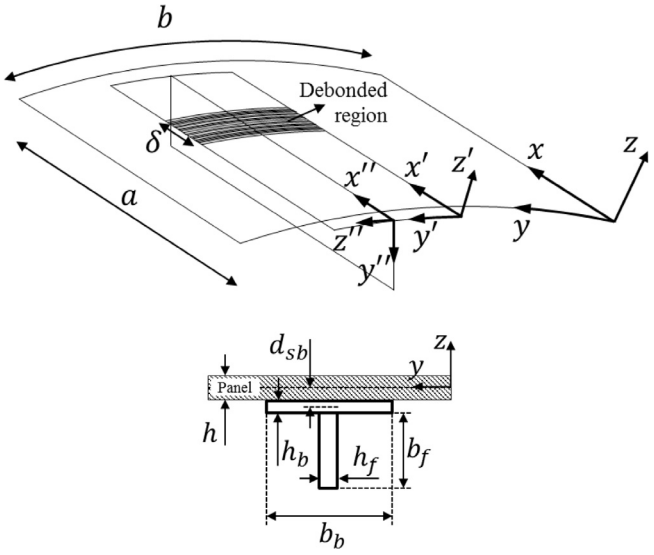


**Fig. 1.** T-Stiffened Panel.

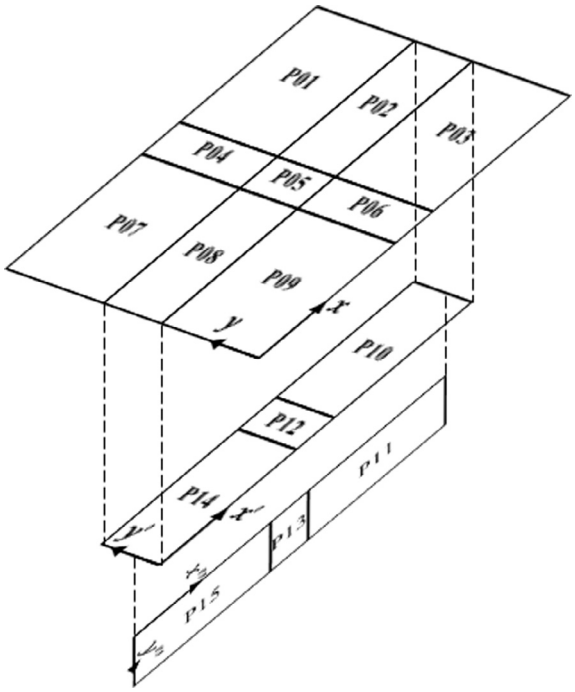


**Fig. 2.** Assembly scheme for semi-analytical models.

assembly is accomplished using connection matrices based on compatibility relations. The unsuccessful single domain approach could theoretically be improved by higher order polynomials, but the 24th order polynomials already started to become computationally expensive and prone to numerical instability with a numerical precision of 64-bits (double), whereas the multi-domain approach allows the use of considerably lower order polynomials for each domain, keeping the computational cost low and the numerical stability high even for complex and displacement fields, verified nearby the debonded region. Note that in the assembly scheme of Fig. 2 the debonded region is the connection between panels P05 and P12, and the defect is produced when this connection is omitted. Since non-linear analyses are not performed in the current study, contacts between panels P05, P12 and P13 at

the debonding region are not monitored, and the linear buckling or vibration results are expected to show modes where these panels inter-penetrate, as for the finite element model used in the verifications.

In the assembly configuration of Fig. 2 four compatibility relations are necessary and are defined in Eqs. (1)–(4) for the CLPT.

$$(p_i \leftrightarrow p_j)_{xcte} \begin{cases} u = u \\ v = v \\ w = w \\ w_{,x} = w_{,x} \end{cases} \quad (at\ constant\ x) \tag{1}$$

$$(p_i \leftrightarrow p_j)_{ycte} \begin{cases} u = u \\ v = v \\ w = w \\ w_{,y} = w_{,y} \end{cases} \quad (at\ constant\ y) \tag{2}$$

$$skin_{bot} \leftrightarrow base_{top} \begin{cases} u_{bot} = u'_{top} \\ v_{bot} = v'_{top} \\ w_{bot} = w'_{top} \end{cases} \quad (over\ area) \tag{3}$$

$$base \leftrightarrow flange \begin{cases} u' = u'' \\ v' = w'' \\ w' = -v'' \\ w'_{,y'} = w''_{,y''} \end{cases} \quad (at\ constant\ y) \tag{4}$$

where $u, v, w$ represent the skin, $u', v', w'$ the base and $u'', v'', w''$ the flange displacements. Displacements $(u, v, w)_{bot}$ are taken at the skin bottom face ($z = -h/2$) whereas $(u', v', w')_{top}$ are taken at the stiffener's base top face ($z' = h_b/2$).

The connection between two panels $p_i$ and $p_j$ at a constant $x$ coordinate ($xcte$) is achieved applying condition $(p_i \leftrightarrow p_j)_{xcte}$ shown in Eq. (1) at $x_i = a_i$ for panel $p_i$ and at $x_j = 0$ for panel $p_j$, as illustrated in Fig. 3-a. Similarly, the connection at constant $y$ ($ycte$) is achieved by applying the condition of Eq. (2) at $y_i = b_i$ for panel $p_i$ and at $y_j = 0$ for panel $p_j$, as illustrated in Fig. 3-b.

Fig. 4 illustrates the $skin_{bot} \leftrightarrow base_{top}$ connection, from where the following relations can be derived:

$$\begin{aligned} u_{bot} &= u + (h/2)w_{,x} \\ v_{bot} &= v + (h/2)w_{,y} \\ w_{bot} &= w \end{aligned} \tag{5}$$

$$\begin{aligned} u'_{top} &= u' - (h_b/2)w'_{,x'} \\ v'_{top} &= v' - (h_b/2)w'_{,y'} \\ w'_{top} &= w' \end{aligned}$$

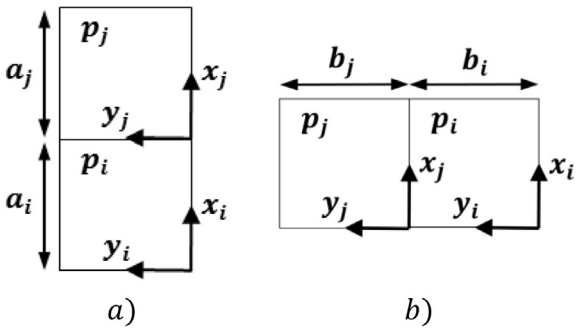


**Fig. 3.** Illustration of connections $(p_i \leftrightarrow p_j)_{xcte}$ and $(p_i \leftrightarrow p_j)_{ycte}$.

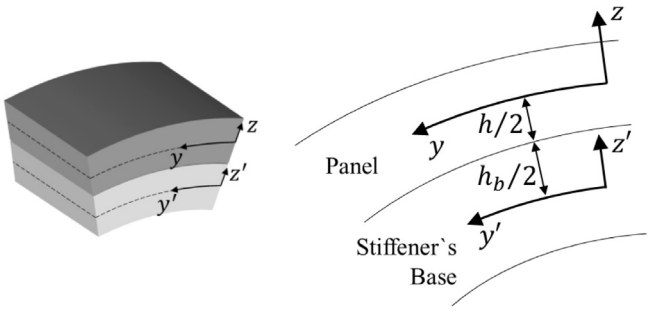


**Fig. 4.** Connection $skin_{bot} \leftrightarrow base_{top}$.

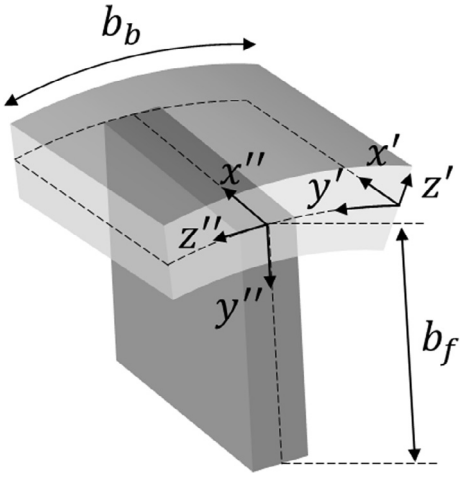


**Fig. 5.** Connection $base \leftrightarrow flange$.

with $u, v, w$ and $u', v', w'$ being the displacements at the skin and stiffener's base mid-surfaces, respectively. Noting that there are no deformations normal to the shell surfaces:

$$\begin{aligned} w_{,x} &= w'_{,x'} \\ w_{,y} &= w'_{,y'} \end{aligned} \tag{6}$$

Applying Eq. (6) in Eq. (5), the connection between the panel and the stiffener's base, cf. Eq. (3), can be written as:

$$\begin{aligned} u' &= u + \tfrac{h}{2}w_{,x} + \tfrac{h_b}{2}w'_{,x'} \\ v' &= v + \tfrac{h}{2}w_{,y} + \tfrac{h_b}{2}w'_{,y'} \\ w' &= w \end{aligned} \tag{7}$$

Connection $base \leftrightarrow flange$, cf. Eq. (4), is illustrated in Fig. 5, where a connection at the mid-surface is assumed between the stiffener's base and flange. The connection is performed by applying Eq. (4) for each stiffener's base segment (P10, P12 and P14) at $y' = b_b/2$, and for each respective stiffener's flange segment (P11, P13 and P15) at $y'' = 0$.

Table 1 summarizes all connection pairs and the respective connection types.

### 2.1. Compatibility equations using natural coordinates

In order to apply the hierarchical polynomials that will be presented in Section 5 as approximation functions, natural coordinate systems must be used and Fig. 6 shows a cylindrical panel with radius $r$ with a cylindrical and a curved natural coordinate system that correlate using Eq. (8).

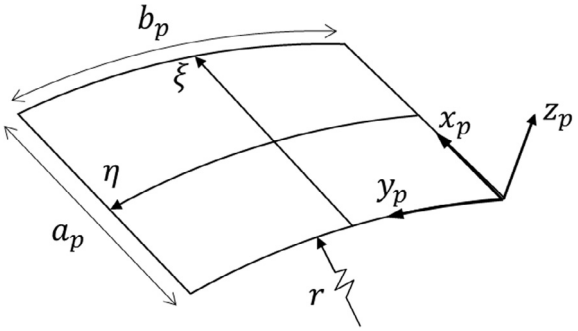


**Fig. 6.** Cartesian system for panel using natural coordinates.

$$\begin{aligned}\xi &= \tfrac{2x_p}{a_p} - 1\\ \eta &= \tfrac{2y_p}{b_p} - 1\end{aligned} \tag{8}$$

Applying the variable transformation of Eq. (8) to Eq. (6) leads to:

$$\begin{aligned} w_{,x} = w'_{,x'} \quad &\rightarrow \quad w_{,\xi} = w'_{,\xi'}\\ w_{,y} = w'_{,y'} \quad &\rightarrow \quad \tfrac{b_b}{b} w_{,\eta} = w'_{,\eta'}\end{aligned} \tag{9}$$

such that the $skin_{bot} \leftrightarrow base_{top}$ compatibility that connects the skin panel to the stiffener's base can be written as:

$$\begin{aligned} u' &= u + \tfrac{2d_{sb}}{a} w_{,\xi}\\ v' &= v + \tfrac{2d_{sb}}{b} w_{,\eta}\\ w' &= w\\ d_{sb} &= h/2 + h_b/2\end{aligned} \tag{10}$$

The other three compatibilities: $(p_i \leftrightarrow p_j)_{xcte}$, $(p_i \leftrightarrow p_j)_{ycte}$ and $base \leftrightarrow flange$ are not affected by the variable transformation of Eq. (8).

## 3. Linear buckling equations

The general eigenproblems for linear buckling [24] is derived using the Neutral Equilibrium Criterion, which states that:

$$\delta^2 W = 0 \tag{11}$$

at a neutral equilibrium point of a minimum or maximum, where $W$ is the total potential energy of the system, defined as:

$$W = \sum U_p + U_{connections} + V \tag{12}$$

with $U_p$ is the strain energy of a given panel in the assembly of Fig. 2; $U_{connections}$ contains the penalty terms that result when the connections of Eqs. (1)–(4) are applied and will be further discussed in Section 6; $V$ is the energy due to the external work, required to determine actual stress state, detailed in Section 3.1.

Integrating over the natural domain $\xi, \eta$ of Fig. 6 using the variable transformation of Eq. (8), the strain energy of a given panel ($U_p$) can be written as:

$$U_p = \left(\frac{a_p b_p}{4}\right) \int_\xi \int_\eta (\boldsymbol{\varepsilon}_\mathbf{p}^\mathbf{T} \boldsymbol{N}_p + \boldsymbol{\kappa}_\mathbf{p}^\mathbf{T} \boldsymbol{M}_\mathbf{p}) d\xi d\eta \tag{13}$$

where for each panel the following relation exists between the strain field $\boldsymbol{\varepsilon}_\mathbf{p}$, $\boldsymbol{\kappa}_\mathbf{p}$ and the membrane force $\boldsymbol{N}_\mathbf{p}$ and bending moment $\boldsymbol{M}_\boldsymbol{p}$ fields:

$$\begin{aligned} \begin{bmatrix} \boldsymbol{N}_\boldsymbol{p} \\ \boldsymbol{M}_\boldsymbol{p} \end{bmatrix} &= \boldsymbol{F}_\boldsymbol{p} \begin{bmatrix} \boldsymbol{\varepsilon}_\boldsymbol{p} \\ \boldsymbol{\kappa}_\boldsymbol{p} \end{bmatrix}\\ \boldsymbol{F}_\boldsymbol{p} &= \begin{bmatrix} \boldsymbol{A} & \boldsymbol{B} \\ \boldsymbol{B} & \boldsymbol{D} \end{bmatrix}\end{aligned} \tag{14}$$

with:

$$\begin{aligned} &\boldsymbol{N}_\mathbf{p}^\boldsymbol{T} = \{\, N_{xx} \quad N_{yy} \quad N_{xy} \,\} \quad \boldsymbol{M}_\mathbf{p}^\boldsymbol{T} = \{\, M_{xx} \quad M_{yy} \quad M_{xy} \,\}\\ &(A_{ij}, B_{ij}, D_{ij}) = \sum_{k=1}^{n_{plies}} \int_{z_k}^{z_{k+1}} \bar{Q}_{ij}^{(k)} (1, z, z^2) dz\end{aligned} \tag{15}$$

and $\bar{Q}_{ij}^{(k)}$ given in Appendix A.

Eq. (16) presents the kinematic equations for a given panel of the assembly of Fig. 2, derived using the Classical Laminated Theory (CLT) [25] with Donnell-type of shell equations [26]:

$$\begin{aligned} &\boldsymbol{\varepsilon}_\mathbf{p}^\boldsymbol{T} = \{\, \varepsilon_{xx}^{(0)} \quad \varepsilon_{yy}^{(0)} \quad \gamma_{xy}^{(0)} \,\}\\ &\boldsymbol{\kappa}_\mathbf{p}^\boldsymbol{T} = \{\, \kappa_{xx} \quad \kappa_{yy} \quad \kappa_{xy} \,\}\\ &\varepsilon_{xx}^{(0)} = \left(\tfrac{2}{a_p}\right) u_{,\xi} + \left(\tfrac{2}{a_p^2}\right) w_{,\xi}^2 \quad \varepsilon_{yy}^{(0)} = \left(\tfrac{2}{b_p}\right) v_{,\eta} + flag_{cyl} \tfrac{1}{r} w + \left(\tfrac{2}{b_p^2}\right) w_{,\eta}^2\\ &\gamma_{xy}^{(0)} = \left(\tfrac{2}{b_p}\right) u_{,\eta} + \left(\tfrac{2}{a_p}\right) v_{,\xi} + \left(\tfrac{4}{a_p b_p}\right) w_{,\xi} w_{,\eta} \kappa_{xx} = -\left(\tfrac{4}{a_p^2}\right) w_{,\xi\xi}\\ &\kappa_{yy} = -\left(\tfrac{4}{b_p^2}\right) w_{,\eta\eta} \quad \kappa_{xy} = -2\left(\tfrac{4}{a_p b_p}\right) w_{,\xi\eta}\end{aligned} \tag{16}$$

where $flag_{cyl} = 1$ for the skin panels and the stiffener's base, both cylindrical panels; and $flag_{cyl} = 0$ for the stiffener's flange, modeled as a flat panel. Using the Ritz Method, the displacement field vector for each panel $\boldsymbol{u_p}$ is approximated as [1]:

$$\begin{aligned} \mathbf{u_p} &= \boldsymbol{S}\, \boldsymbol{c_p}\\ \boldsymbol{u_p} &= \begin{bmatrix} \boldsymbol{u} \\ \boldsymbol{v} \\ \boldsymbol{w} \end{bmatrix} \boldsymbol{S} = \begin{bmatrix} \boldsymbol{S^u} \\ \boldsymbol{S^v} \\ \boldsymbol{S^w} \end{bmatrix}\end{aligned} \tag{17}$$

where $\boldsymbol{S^u}$, $\boldsymbol{S^v}$ and $\boldsymbol{S^w}$ are sub-matrices with 1 row and $3 \times m \times n$ columns containing the shape of the approximation functions for $u$, $v$ and $w$, respectively; $\boldsymbol{c_p}$ is a vector of size $3 \times m \times n$ containing the amplitude of each term in the approximation function. Constants $m$ and $n$ determine how many approximation terms are required along $x$ and y, respectively; or along $\xi$ and $\eta$ when natural coordinates are used.

Using the approximation of Eq. (17), the kinematic relations of Eq. (16) can conveniently be written in matrix form as [25–28]:

$$\begin{aligned} \boldsymbol{\varepsilon_p} &= (\boldsymbol{B_{0_p}} + \tfrac{1}{2} \boldsymbol{B_{L_p}}) \boldsymbol{c_p}\\ \boldsymbol{\kappa_p} &= \boldsymbol{B_{\kappa_p}} \boldsymbol{c_p}\end{aligned} \tag{18}$$

such that:

$$\begin{aligned} \boldsymbol{B_{0_p}} &= \begin{bmatrix} \left(\tfrac{2}{a_p}\right) \tfrac{\partial \boldsymbol{S^u}}{\partial \xi} \\ \left(\tfrac{2}{b_p}\right) \tfrac{\partial \boldsymbol{S^v}}{\partial \eta} + flag_{cyl} \tfrac{1}{r} \boldsymbol{S^w} \\ \left(\tfrac{2}{b_p}\right) \tfrac{\partial \boldsymbol{S^u}}{\partial \eta} + \left(\tfrac{2}{a_p}\right) \tfrac{\partial \boldsymbol{S^v}}{\partial \xi} \end{bmatrix} \quad \boldsymbol{B_{\kappa_p}} = \begin{bmatrix} -\left(\tfrac{4}{a_p^2}\right) \tfrac{\partial^2 \boldsymbol{S^w}}{\partial \xi^2} \\ -\left(\tfrac{4}{b_p^2}\right) \tfrac{\partial^2 \boldsymbol{S^w}}{\partial \eta^2} \\ -2\left(\tfrac{4}{a_p b_p}\right) \tfrac{\partial^2 \boldsymbol{S^w}}{\partial \xi \partial \eta} \end{bmatrix}\\ \boldsymbol{B_{L_p}} &= \begin{bmatrix} \left(\tfrac{4}{a_p^2}\right) w_{,\xi} \tfrac{\partial \boldsymbol{S^w}}{\partial \xi} \\ \left(\tfrac{4}{b_p^2}\right) w_{,\eta} \tfrac{\partial \boldsymbol{S^w}}{\partial \eta} \\ \left(\tfrac{4}{a_p b_p}\right) \left(w_{,\xi} \tfrac{\partial \boldsymbol{S^w}}{\partial \eta} + w_{,\eta} \tfrac{\partial \boldsymbol{S^w}}{\partial \xi}\right) \end{bmatrix}\end{aligned} \tag{19}$$

Note that matrix $\boldsymbol{B_{L_p}}$ contains non-linear terms that become important in analyses with large displacements, but in the current study are only required to derive the geometric stiffness matrix. Using the definitions of Eq. (19) it is possible to apply the same derivation of Castro et al. [29] to solve the neutral equilibrium criterion of Eq. (11), resulting in the following generalized eigenvalue problem:

$$(\boldsymbol{K} + \lambda_{CR}\boldsymbol{K_G})\boldsymbol{c} = \{0\} \tag{20}$$

where $\boldsymbol{K}$ is the global constitutive stiffness matrix, $\boldsymbol{K_G}$ the global geometric stiffness matrix and $c$ the global set of Ritz constants that define the approximation functions for all panels in the assembly of Fig. 2, $\lambda_{CR}$ a scalar load multiplier that renders the instability condition of Eq. (20). There are as many $\lambda_{CR}$, $\boldsymbol{c}$ pairs as there are independent approximation terms describing the displacement field variables. Matrix $\boldsymbol{K}$ is assembled as:

$$\boldsymbol{K} = \begin{bmatrix} \boldsymbol{K_{P01}} & & & 0 \\ & \boldsymbol{K_{P02}} & & \\ & & \ddots & \\ sym & & & \boldsymbol{K_{P15}} \end{bmatrix} \tag{21}$$

where $\boldsymbol{K_{P01}}$ is the constitutive matrix of panel P01, $\boldsymbol{K_{P02}}$ of panel P02 and so forth.

The constitutive stiffness matrix of a given panel, $\boldsymbol{K_p}$, is calculated with:

$$\boldsymbol{K_p} = \left(\frac{a_p b_p}{4}\right) \int_\xi \int_\eta \boldsymbol{B_{0_p}^{T^{ij}}} \boldsymbol{F_p} \boldsymbol{B_{0_p}^{k\ell}} d\xi d\eta \tag{22}$$

where indices $i, j$ define the row-wise and $k, \ell$ the column-wise position within the matrix.

The global geometric stiffness matrix $\boldsymbol{K_G}$ is assembled similarly to $\boldsymbol{K}$, cf. Eq. (21), and the contribution of each panel is defined as:

$$\boldsymbol{K_{G_p}} = \left(\frac{a_p b_p}{4}\right) \int_\xi \int_\eta \boldsymbol{G_p^{T^{ij}}} \begin{bmatrix} N_{xx} & N_{xy} \\ N_{xy} & N_{yy} \end{bmatrix} \boldsymbol{G_p^{k\ell}} d\xi d\eta \tag{23}$$

with $\boldsymbol{G_p}$ computed for each panel as:

$$\boldsymbol{G_p} = \begin{bmatrix} \left(\frac{2}{a_p}\right) \frac{\partial \boldsymbol{S^w}}{\partial \xi} \\ \left(\frac{2}{b_p}\right) \frac{\partial \boldsymbol{S^w}}{\partial \eta} \end{bmatrix} \tag{24}$$

Appendix B gives the detailed expressions needed to calculate $\boldsymbol{K_p}$ in Eq. (B.1) and $\boldsymbol{K_{G_p}}$ in Eq. (B.2).

### 3.1. Loading and boundary conditions

Fig. 7 illustrates the axial compression load and the boundary conditions applied to six edges of the panel assembly model. Note that stiffened panel is under a load-controlled axial compression where the compressive load is applied at one edge of the skin (panels P07, P08 and P09) and at one edge of the stiffener's base (panel P14) and one edge of the stiffener's flange (panel P15); with all these edges free to move along the load direction (parallel to the stiffener).

Due to the load configuration of Fig. 7 the following external energy term can be defined for panels P07, P08 and P09:

$$\boldsymbol{V}_{skin} = \frac{b_p}{2} \boldsymbol{N}_{xx} \int_\eta \boldsymbol{S^u} d\eta \boldsymbol{c_p} \tag{25}$$

where $b_p$ is the width (along $y$) of the corresponding panel. Generalizing, the contribution of each panel to the external work is:

$$V_p = \boldsymbol{c_p^T} \boldsymbol{f_{ext_p}} \tag{26}$$

where $\boldsymbol{f_{ext_p}}$ is the external force vector and $\boldsymbol{c_p}$ the local set of unknown Ritz constants, both for a given panel "$p$".

The load scheme of Fig. 7 will result in a non-constant membrane stress state and therefore the initial stress stiffness matrix $\boldsymbol{K_G}$ is computed numerically, where for each integration point the actual membrane stress state is obtained based on linear static analysis using following system of equations:

$$\boldsymbol{f_{ext}} = \boldsymbol{K}\boldsymbol{c} \tag{27}$$

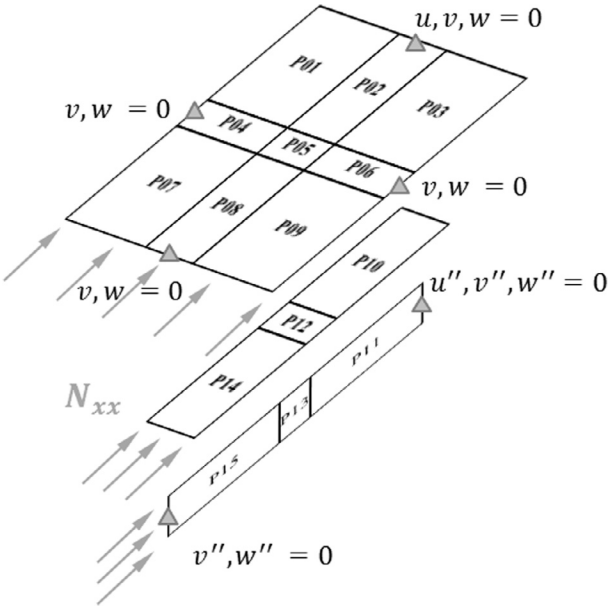


**Fig. 7.** Load and boundary condition for linear buckling analysis.

where $\boldsymbol{c}$ is the unknown global set of Ritz constants. For each integration point within each panel the local set of Ritz constants $\boldsymbol{c_p}$, directly obtained from $\boldsymbol{c}$, is applied to compute the strains as per Eq. (18), which are then used to compute the stresses using Eq. (14). The calculated membrane stresses $N_{xx}$, $N_{yy}$ and $N_{xy}$ are finally used in Eq. (B.2) to compute $\boldsymbol{K_{G_p}}$. Legendre-Gauss quadrature [30] was used to obtain the integration points' positions and weights and a convergence analysis was performed in order to show the minimum quadrature order that should be used.

Fig. 7 also shows how the boundary conditions are distributed for the skin and stiffener. The skin edges that move along $x$ due to the applied load have $v = w = 0$ and the edge passing through panels P01, P02 and P03 have $u = v = w = 0$. The stiffener's base has all edges free and the flange has $v'' = w'' = 0$ at the loaded edge and $u'' = v'' = w'' = 0$ at the unloaded edge. Despite having all edges free, the stiffener's base has the support from all adjacent panels in the assembly.

## 4. Free vibration equations

The harmonic natural frequency analysis consists on the following generalized eigenproblem [31]:

$$(\boldsymbol{K} - \omega^2 \boldsymbol{M})\boldsymbol{c} = \{0\} \tag{28}$$

where $\boldsymbol{K}$ is the constitutive stiffness matrix, $\boldsymbol{M}$ is the mass matrix, $\omega$ is the angular frequency that corresponds to the vibration mode calculated using $\boldsymbol{c}$ and the approximation functions. The mass matrix $\boldsymbol{M}$ is assembled similarly to $\boldsymbol{K}$, cf. Eq. (21), and computed using Eq. (B.3).

Fig. 8 illustrates the boundary conditions that were applied for the vibration analysis, where the skin is restrained at the four edges by $u = v = w = 0$, the stiffener's base with all edges free and the flange with $u'' = v'' = w'' = 0$ at both extremity edges. Despite the stiffener's base has its edges free, its proper support is guaranteed by the adjacent structures in the assembly.

## 5. Approximation functions

Vescovini and Bisagni [17] presented a semi-analytical model for omega stiffened panels using trigonometric approximation

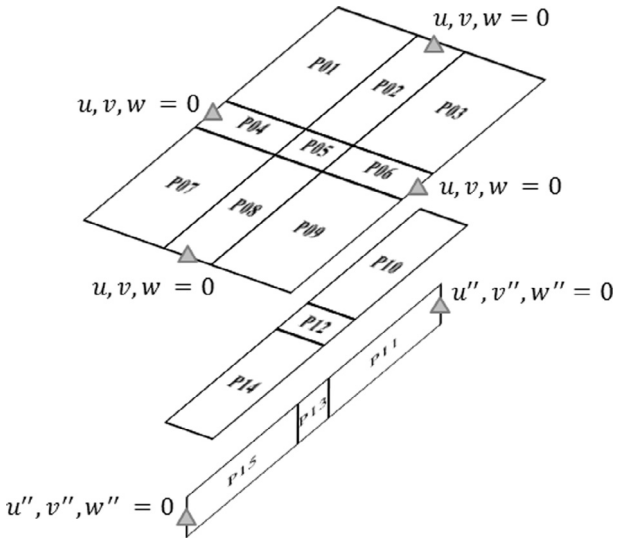


**Fig. 8.** Boundary condition for vibration analysis.

functions, valid for local buckling predictions where no displacement occurs at the connection and only the rotations must be coupled. The use of more flexible approximation functions such as the Legendre polynomials herein explored permits the generalization of the modelling approach presented by Vescovini and Bisagni, allowing any displacement and rotation coupling at the interfaces between adjacent panels, which are necessary to achieve the proposed assembly of Fig. 2.

Rodrigues derived a form of Legendre hierarchic orthogonal polynomials [32,33] largely applied by Bardell et al. on the vibration problems [34–36]. In this form the first four terms $i = 1,2,3,4$ consist of Hermite cubic polynomials:

$$\begin{aligned} s_{i=1}(\xi \text{ or } \eta) &= \left(\tfrac{1}{2} - \tfrac{3}{4}\xi + \tfrac{1}{4}\xi^3\right) flag_{t1} \\ s_{i=2}(\xi \text{ or } \eta) &= \left(\tfrac{1}{8} - \tfrac{1}{8}\xi - \tfrac{1}{8}\xi^2 + \tfrac{1}{8}\xi^3\right) flag_{r1} \\ s_{i=3}(\xi \text{ or } \eta) &= \left(\tfrac{1}{2} + \tfrac{3}{4}\xi - \tfrac{1}{4}\xi^3\right) flag_{t2} \\ s_{i=4}(\xi \text{ or } \eta) &= \left(-\tfrac{1}{8} - \tfrac{1}{8}\xi + \tfrac{1}{8}\xi^2 + \tfrac{1}{8}\xi^3\right) flag_{r2} \end{aligned} \tag{29}$$

Flags $flag_{t1}$, $flag_{r1}$, $flag_{t2}$ and $flag_{r2}$ will always be 0 or 1. Using these flags the first four terms of Rodrigues polynomials can be used to enable/disable the translation and rotation of each domain boundary. Flag $flag_{t1}$ is used to control the translation at boundary 1 ($\xi = -1$), which is possible because using Rodrigues polynomials this is the only term among all terms in the approximation function that produces $s_i(\xi = -1) = 1$. Similarly, $flag_{t2}$ is used to control the translation at boundary 2 ($\xi = +1$). The rotation at $\xi = -1$ and $\xi = +1$ is respectively controlled using $flag_{r1}$ and $flag_{r2}$, since they are the only terms that produce a non-null rotation $\partial s/\partial\xi$ at each respective domain boundary. A detailed overview of the produced shape functions is given by Bardell [34].

All terms with $i > 4$ are higher order K-orthogonal hierarchic polynomials that always generate null translation ($s_i = 0$) and null rotation ($\partial s_i/\partial\xi = 0$) at both extremities ($\xi = -1$ or $\xi = +1$), defined as:

$$s_{i>4}(\xi \text{ or } \eta) = \sum_{p=0}^{i/2} \frac{(-1)^p (2i-2p-7)!!}{2^p p!(i-2p-1)!}\xi^{i-2p-1} \tag{30}$$

where $!q = q(q-2)\ldots(2 or 1)0!! = (-1)!! = 1$ and $i/2$ in the summation is an integer division.

Rodrigues' form of Legendre's polynomials can be directly applied as approximation functions for domains expressed in natural coordinates like the one shown in Fig. 6, with $i = 1,2,3,\ldots,m$ terms along coordinate $\xi$ and $j = 1,2,3,\ldots,n$ terms along coordinate $\eta$. Given that all boundary conditions required for each panel in the assemblies of Figs. 7 and 8 can be achieved using the flags of Eq. (29), it is possible to use the same set of shape functions for $u$, $v$ and $w$, being also the same for either $\xi$ or $\eta$.

The fact that the same set of shape functions can be used for all panels and for all displacement field variables facilitates the analytical integration of the matrices given in Eqs. (B.1) and (B.3) regarding that constant constitutive properties are used within each panel domain. No publication dealing with the analytical integration of the constitutive and connectivity matrices for the analysis of stiffened panels using Rodrigues' modification on Legendre hierarchic polynomials has been found in the literature. In the current implementation [37] the analytical integrations are performed as shown in Eq. (31), where it is demonstrated how to separate the terms depending on $\xi$ and $\eta$. After every $ik$ (or $j\ell$) combinations are calculated, they are stored in lookup tables such that the stiffness matrices are efficiently integrated.

$$\begin{aligned} u_{,\xi}^{ij} &= c_{ij}^u \tfrac{\partial f_i^u(\xi)}{\partial\xi} g_j^u(\eta) \\ v_{,\eta}^{k\ell} &= c_{k\ell}^v f_k^v(\xi) \tfrac{\partial g_\ell^v(\eta)}{\partial\eta} \\ u_{,\xi}^{ij} v_{,\eta}^{k\ell} &= c_{ij}^u c_{k\ell}^v f_{i,\xi}^u(\xi) f_k^v(\xi) g_j^u(\eta) g_{\ell,\eta}^v(\eta) \\ \int_\xi \int_\eta u_{,\xi}^{ij} v_{,\eta}^{k\ell} d\xi d\eta &= c_{ij}^u c_{k\ell}^v \int_\xi f_{i,\xi}^u(\xi) f_k^v(\xi) d\xi \int_\eta g_j^u(\eta) g_{\ell,\eta}^v(\eta) d\eta \end{aligned} \tag{31}$$

where $c_{ij}$ and $c_{k\ell}$ represent Ritz constants.

## 6. Penalty approach for the assembly

The compatibilities of Eqs. (1)–(4) are imposed using a penalty approach, where the penalty energy terms for each case are, respectively:

$$\begin{aligned} U_{p_i p_{j_{xcte}}} &= \left(\tfrac{b_{p_i}}{2}\right) \int_\eta k_t^{c1} \Big[ (u_i - u_j)^2 + (v_i - v_j)^2 + (w_i + w_j)^2 \\ &\quad + \left(\tfrac{2}{a_{p_i}} w_{,\xi_i} - \tfrac{2}{a_{p_j}} w_{,\xi_j}\right)^2 k_r^{c1}/k_t^{c1} \Big] d\eta \\ U_{p_i p_{j_{ycte}}} &= \left(\tfrac{a_{p_i}}{2}\right) \int_\xi k_t^{c2} \Big[ (u_i - u_j)^2 + (v_i - v_j)^2 + (w_i + w_j)^2 \\ &\quad + \left(\tfrac{2}{b_{p_i}} w_{,\eta_i} - \tfrac{2}{b_{p_j}} w_{,\eta_j}\right)^2 k_r^{c2}/k_t^{c2} \Big] d\xi \\ U_{p_{i_{bot}} p_{j_{top}}} &= \left(\tfrac{a_{p_i} b_{p_i}}{4}\right) \int_\xi \int_\eta k_t^{c3} \Big[ \left( \left( u + \tfrac{2d_{ij}}{a_{p_i}} w_{,\xi} \right) - u' \right)^2 \\ &\quad + \left( \left( v + \tfrac{2d_{ij}}{b_{p_i}} w_{,\eta} \right) - v' \right)^2 + (w - w')^2 \Big] d\xi d\eta \\ U_{bf} &= \left(\tfrac{a}{2}\right) \int_\xi k_t^{c4} \Big[ (u' - u'')^2 + (v' - w'')^2 + (w' + v'')^2 \\ &\quad + \left(\tfrac{2}{b_b} w'_{,\eta'} - \tfrac{2}{b_f} w''_{,\eta''}\right)^2 k_r^{c4}/k_t^{c4} \Big] d\xi \end{aligned} \tag{32}$$

with $k_t^{ci}$ and $k_r^{ci}$ being constant translational and rotational penalty stiffnesses; subscripts $p_i$ and $p_j$ indicate the panels being connected. The energy terms of Eq. (32) are added to the global constitutive stiffness matrix $\boldsymbol{K}$ according to the connectivity scheme of Table 1.

Theoretically, the penalty stiffnesses $k_t^{ci}$ and $k_r^{ci}$ can be arbitrarily high in order to impose the energy penalty. However, the use of high values is associated with numerical instabilities such that one should choose the penalty stiffnesses that are just high enough to impose the proper penalties, but not excessively high. In the current study it is proposed to calculate $k_t^{ci}$ and $k_r^{ci}$ based on laminate properties of the panels being connected, instead of using fixed high values, a common practice in the literature.

**Table 1**
Connectivity types.

| Location | Pair | Connection | Location | Pair | Connection |
|---|---|---|---|---|---|
| Skin-Skin | P01 ↔ P02 | $(p_i \leftrightarrow p_j)_{ycte}$ | Skin-Skin | P08 ↔ P09 | $(p_i \leftrightarrow p_j)_{ycte}$ |
| Skin-Skin | P01 ↔ P04 | $(p_i \leftrightarrow p_j)_{xcte}$ | Skin-Base | P02 ↔ P10 | $skin_{bot} \leftrightarrow base_{top}$ |
| Skin-Skin | P02 ↔ P03 | $(p_i \leftrightarrow p_j)_{ycte}$ | Skin-Base | P05 ↔ P12 | Debonded |
| Skin-Skin | P02 ↔ P05 | $(p_i \leftrightarrow p_j)_{xcte}$ | Skin-Base | P08 ↔ P14 | $skin_{bot} \leftrightarrow base_{top}$ |
| Skin-Skin | P03 ↔ P06 | $(p_i \leftrightarrow p_j)_{xcte}$ | Base-Base | P10 ↔ P12 | $(p_i \leftrightarrow p_j)_{xcte}$ |
| Skin-Skin | P04 ↔ P05 | $(p_i \leftrightarrow p_j)_{ycte}$ | Base-Base | P12 ↔ P14 | $(p_i \leftrightarrow p_j)_{xcte}$ |
| Skin-Skin | P04 ↔ P07 | $(p_i \leftrightarrow p_j)_{xcte}$ | Base-Flange | P10 ↔ P11 | $base \leftrightarrow flange$ |
| Skin-Skin | P05 ↔ P06 | $(p_i \leftrightarrow p_j)_{ycte}$ | Base-Flange | P12 ↔ P13 | $base \leftrightarrow flange$ |
| Skin-Skin | P05 ↔ P08 | $(p_i \leftrightarrow p_j)_{xcte}$ | Base-Flange | P14 ↔ P15 | $base \leftrightarrow flange$ |
| Skin-Skin | P06 ↔ P09 | $(p_i \leftrightarrow p_j)_{xcte}$ | Flange-Flange | P11 ↔ P13 | $(p_i \leftrightarrow p_j)_{xcte}$ |
| Skin-Skin | P07 ↔ P08 | $(p_i \leftrightarrow p_j)_{ycte}$ | Flange-Flange | P13 ↔ P15 | $(p_i \leftrightarrow p_j)_{xcte}$ |

All penalty stiffnesses are calculated assuming that the membrane and bending loads $N_{xx}$, $N_{yy}$, $M_{xx}$ and $M_{yy}$ are continuous from one panel to another, and that the compatibility of strains is such that the strain at the connection is assumed to be the average between the strains at the adjacent panels. Four strain compatibility scenarios are used, as presented in Eq. (33).

$$\begin{aligned} &a)\ \frac{\varepsilon_{xx}^{p_i}+\varepsilon_{xx}^{p_j}}{2}=\varepsilon_{xx}^{conn} \quad b)\ \frac{\kappa_{xx}^{p_i}+\kappa_{xx}^{p_j}}{2}=\kappa_{xx}^{conn} \\ &c)\ \frac{\varepsilon_{yy}^{p_i}+\varepsilon_{yy}^{p_j}}{2}=\varepsilon_{yy}^{conn} \quad d)\ \frac{\kappa_{yy}^{p_i}+\kappa_{yy}^{p_j}}{2}=\kappa_{yy}^{conn} \end{aligned} \tag{33}$$

The compatibility of Eq. (33)-a is used to compute $k_t^{c1}$. For both panels the simplification $\varepsilon_{xx}=N_{xx}/A_{11}$ is assumed, with $A_{11}$ defined in Eq. (15). From a dimensional analysis of Eq. (32) the units of $k_t^{c1}$ must be $[F/L^2]$, such that the strain at the connection can be stated as $\varepsilon_{xx}^{conn}=N_{xx}/(k_t^{c1}h)$, where $h$ will be taken as the average thickness of both panels of the connection. Holding these assumptions, the compatibility of Eq. (33)-a gives:

$$\begin{aligned} &\frac{N_{xx}}{2A_{11}^{p_i}}+\frac{N_{xx}}{2A_{11}^{p_j}}=\frac{N_{xx}}{k_t^{c1}\left(\frac{h^{p_i}+h^{p_j}}{2}\right)} \\ &k_t^{c1}=\frac{4A_{11}^{p_i}A_{11}^{p_j}}{(A_{11}^{p_i}+A_{11}^{p_j})(h^{p_i}+h^{p_j})} \end{aligned} \tag{34}$$

With similar assumptions and using Eq. (33)-b with $\kappa_{xx}^{conn}=M_{xx}/(k_r^{c1}h)$ and for both panels using $\kappa_{xx}=M_{xx}/D_{11}$, with $D_{11}$ defined in Eq. (15); $k_r^{c1}$ can be computed as:

$$k_r^{c1}=\frac{4D_{11}^{p_i}D_{11}^{p_j}}{(D_{11}^{p_i}+D_{11}^{p_j})(h^{p_i}+h^{p_j})} \tag{35}$$

To compute $k_t^{c2}$ and $k_r^{c2}$, which respectively have the same units of $k_t^{c1}$ and $k_r^{c1}$, the procedure is carried out using Eq. (33)-c and (33)-d, with the assumptions $\varepsilon_{yy}=N_{yy}/A_{22}$ and $\kappa_{yy}=M_{yy}/D_{22}$, resulting in:

$$k_t^{c2}=\frac{4A_{22}^{p_i}A_{22}^{p_j}}{(A_{22}^{p_i}+A_{22}^{p_j})(h^{p_i}+h^{p_j})} \tag{36}$$

and:

$$k_r^{c2}=\frac{4D_{22}^{p_i}D_{22}^{p_j}}{(D_{22}^{p_i}+D_{22}^{p_j})(h^{p_i}+h^{p_j})} \tag{37}$$

From Eq. (32) the units of $k_t^{c3}$ must be $[N/m^3]$ and since the connection consists of normal loads acting on the shell, the compatibility relations of Eq. (33) no longer apply. In this case $k_t^{c1}$ is used, with a dimensional correction:

$$k_t^{c3}=\frac{k_t^{c1}}{min(a_p,b_p)} \tag{38}$$

where $a_p$ and $b_p$ are illustrated in Fig. 6.

Finally, $k_t^{c4}$ and $k_r^{c4}$ used at the connection between the stiffener's base and stiffener's flange are assumed to be the same as $k_t^{c2}$ and $k_r^{c2}$, respectively, giving:

$$k_t^{c4}=k_t^{c2} \tag{39}$$

and:

$$k_r^{c4}=k_r^{c2} \tag{40}$$

Penalty constants $k_t^{ci}$ and $k_r^{ci}$ calculated as herein suggested showed to provide numerically stable results for a wide range of inputs, with Legendre polynomial orders up to 25th, which is the highest order tested by the authors.

## 7. Results

Following analyses correspond to various values of $a/b$ and $b/b_b$, fixing $b_b=2b_f$ and $b$ = 1 m . The orthotropic laminae properties are $E_1=142.5$ GPa, $E_2=8.7$ GPa, $\nu_{12}=0.28$, $G_{12}=5.1$ GPa with a ply thickness of $1.25\times10^{-4}$ m. The detailed discussion presented along this section is based on the results obtained for the stiffened panels shown in Table 2. The applied debonding defect is centered at $x=a/2$ for all investigated cases.

### 7.1. Convergence of the numerical integration scheme

The geometric stiffness matrix representing the pre-buckling state is calculated by integrating Eq. (23). An analytical integration is straightforward when each panel domain has a constant membrane stress state, whereas general stress states require numerical integration. A Legendre-Gauss quadrature [30] rule was chosen and this section shows how the critical buckling load converges with the increase of the quadrature order selected.

Laminate configuration #1 of Table 2 was chosen with the geometry: $a/b=10$; $b_b=b/5$; with a debonding defect of $\delta=0.4a$. An edge load $N_{xx}$ is applied as illustrated in Fig. 7. Fig. 9-a shows the convergence of $N_{xx_{CR}}$ for a flat panel; and Fig. 9-b for a curved panel with $r=10$ m. Note that using a 10th order quadrature rule produces converged linear buckling result for the approximation of each panel domain using up to $m=n=8$ terms. The authors observed that for smaller $a/b$ ratios lower quadrature rule orders can be used to achieved converged results. The 10th order quadrature rule will be used for all results presented in the next sections.

**Table 2**
Laminates for stiffened panels analyzed.

| Stiffened panel | Label | Skin | Base | Flange |
|---|---|---|---|---|
| #1 | – | $[0, \pm 45, 90, \mp 45, 0]$ | $[0, 90, 0]_4$ | $[0, 90, 0]_8$ |
| #2 | Sym angled 45 stiffener 0,90 | $[(\pm 45)_2]_{sym}$ | $[0, 90, 90, 0]_4$ | $[0, 90, 90, 0]_8$ |
| #3 | Angled 45 stiffener 0,90 | $[0_4, (\pm 45)_2]$ | $[0, 90, 90, 0]_4$ | $[0, 90, 90, 0]_8$ |
| #4 | Sym angled 45 stiffener 0,45 | $[(\pm 45)_2]_{sym}$ | $[0, \mp 45, 0]_4$ | $[(0, \mp 45, 0)_4, (0, \pm 45, 0)_4]$ |
| #5 | Angled 45 stiffener 0,45 | $[0_4, (\pm 45)_2]$ | $[0, \mp 45, 0]_4$ | $[(0, \mp 45, 0)_4, (0, \pm 45, 0)_4]$ |
| #6 | Sym angled 30 stiffener 0,90 | $[(\pm 30)_2]_{sym}$ | $[0, 90, 90, 0]_4$ | $[0, 90, 90, 0]_8$ |
| #7 | Angled 30 stiffener 0,90 | $[0_4, (\pm 30)_2]$ | $[0, 90, 90, 0]_4$ | $[0, 90, 90, 0]_8$ |
| #8 | Sym angled 30 stiffener 0,45 | $[(\pm 30)_2]_{sym}$ | $[0, \mp 45, 0]_4$ | $[(0, \mp 45, 0)_4, (0, \pm 45, 0)_4]$ |
| #9 | Angled 30 stiffener 0,45 | $[0_4, (\pm 30)_2]$ | $[0, \mp 45, 0]_4$ | $[(0, \mp 45, 0)_4, (0, \pm 45, 0)_4]$ |
| #10 | Sym angled 60 stiffener 0,90 | $[(\pm 60)_2]_{sym}$ | $[0, 90, 90, 0]_4$ | $[0, 90, 90, 0]_8$ |
| #11 | Angled 60 stiffener 0,90 | $[0_4, (\pm 60)_2]$ | $[0, 90, 90, 0]_4$ | $[0, 90, 90, 0]_8$ |
| #12 | Sym angled 60 stiffener 0,45 | $[(\pm 60)_2]_{sym}$ | $[0, \mp 45, 0]_4$ | $[(0, \mp 45, 0)_4, (0, \pm 45, 0)_4]$ |
| #13 | Angled 60 stiffener 0,45 | $[0_4, (\pm 60)_2]$ | $[0, \mp 45, 0]_4$ | $[(0, \mp 45, 0)_4, (0, \pm 45, 0)_4]$ |

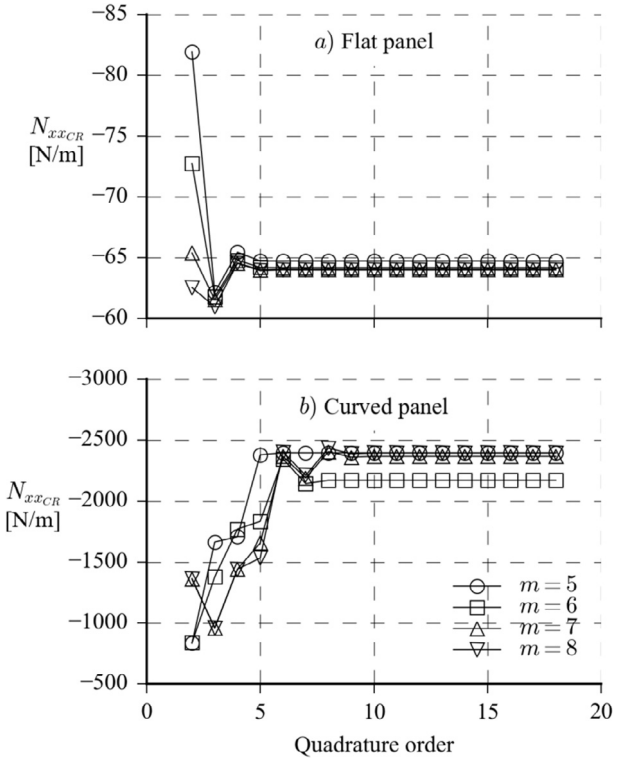


**Fig. 9.** Convergence of the quadrature order.

### 7.2. Linear buckling with different defect lengths

The effect of the defect length $\delta$ on the critical linear buckling load was investigated for various different geometries of the stiffened panel of Fig. 1. NX Nastran was used to provide finite element results, where a mesh size of 0.02 m and linear quadratic elements (CQUAD4) were used, with the same load and boundary conditions explained in Section 3.1. The interface between the skin and the stiffeners' base is rendered using RBE2 elements that are created in rows along $y$, and the variable defect length $\delta$ is produced by removing a desired number RBE2 rows.

Table 3 presents a convergence analysis including a verification against the finite element (FE) model. All errors are relative to the corresponding FE result. Stiffened panel #1 from Table 2 was used in these comparisons with $a/b = 0.5$ and $b/b_b = 5$, where a very good correlation is observed already with $m = n = 5$. Using $m = n = 8$ produced errors of less than 1% for all the range of interest of the defect length ($0 \leqslant \delta/a \leqslant 0.9$), and therefore it will be the precision adopted for the approximated functions in all next studies, unless otherwise specified. Using a similar configuration of Table 3 but adding a curvature of $r = 10$ m to the skin and stiffener's base leads to the convergence results of Table 4, where $m = n = 8$ also produce errors of less than 1% for all range of defect length. For either flat or curved panels with higher $a/b$ the authors verified an even better convergence behavior.

The displacement field and the pre-buckling membrane stress state calculated from static analysis results were compared with finite elements. Stiffened panel #1 Table 2 was chosen with a flat skin, with the geometry: $a/b = 2$; $b/b_b = 5$. Each panel domain is approximated with $m = n = 10$. Fig. 10 compares the pre-buckling displacement field $u$; and Fig. 11 the membrane stress field $N_{xx}$. Two configurations were compared, one with $\delta = 0$ and another with $\delta/a = 0.6$. It can be seen that the displacement field matches exactly whereas the membrane stress field matches very well qualitatively, with differences for $N_{xx_{min}}$ of $-8.1\%$ and $+2.0\%$, respectively for $\delta = 0$ and $\delta/a = 0.6$; and for $N_{xx_{max}}$ of $+0.5\%$ and $-10.1\%$ for $\delta = 0$ and $\delta/a = 0.6$. Note in Fig. 11 that there is a discontinuity of $N_{xx}$ at the interface between panels P02, P05 and P08, indicating that the compatibility equations herein adopted are not guaranteeing a smooth transition of strains and stresses among the domains, despite the displacement transition was verified to be smooth for all cases.

Fig. 12 shows normalized linear buckling results for flat panels using stiffened panel #1 of Table 2 with different $a/b$ and $b/b_b$ ratios, where $N_{xx_{CR}}^{\delta=0}$ is the critical linear buckling load without the debonding defect (i.e. for $\delta/a = 0$). A similar behavior for all three $b/b_b$ ratios is observed and there is a clear degradation of $N_{xx_{CR}}$ for larger defect lengths and the degradation becomes more abrupt for stiffened panels with higher $a/b$ values. The curves also show that higher $a/b$ values will lead to smaller thresholds of critical debonding defect size. Results for the stiffened panel laminates #2 to #15 are very similar to the results for stiffened panel #1 shown in Fig. 12 (cf. Appendix C).

Eigenvector results for different geometry configurations using $b/b_b = 5$ are presented in Fig. 13, where the skin panel domains are identified and their boundaries highlighted in dashed lines. The abrupt reduction of the critical linear buckling load coincides with the change on the critical eigenvector from two semi-waves on each side of the stiffener to one semi-wave centered at the defect region.

From the curves of Fig. 12 and the eigenvectors of Fig. 13 it becomes clear that the reason why higher $a/b$ values lead to smaller debonding defect thresholds is that for such panels the semi-wave centered at the defect region is easily formed.

Eigenvectors for $a/b = 1$ and two defect lengths ($\delta/a = 0.5$ and $\delta/a = 0.9$) from Fig. 13 where verified against eigenvectors

**Table 3**
Convergence and verification with FE analysis, flat panel, linear buckling.

| | $\delta/a$ | 0.000 | 0.200 | 0.400 | 0.600 | 0.807 | 0.907 |
|---|---|---|---|---|---|---|---|
| $m=n=5$ | $N_{xx_{CR}}$ | 6.05 | 6.04 | 5.96 | 5.77 | 5.36 | 5.03 |
| | Error | 1.19% | 1.57% | 2.31% | 3.16% | 3.96% | 3.35% |
| $m=n=6$ | $N_{xx_{CR}}$ | 6.03 | 6.01 | 5.91 | 5.69 | 5.26 | 4.95 |
| | Error | 0.78% | 1.02% | 1.41% | 1.76% | 2.06% | 1.84% |
| $m=n=8$ | $N_{xx_{CR}}$ | 6.01 | 5.98 | 5.86 | 5.63 | 5.20 | 4.89 |
| | Error | 0.43% | 0.51% | 0.60% | 0.67% | 0.74% | 0.52% |
| $m=n=10$ | $N_{xx_{CR}}$ | 6.00 | 5.96 | 5.85 | 5.61 | 5.18 | 4.87 |
| | Error | 0.29% | 0.30% | 0.31% | 0.34% | 0.37% | 0.07% |
| FE | $N_{xx_{CR}}$ | 5.98 | 5.95 | 5.83 | 5.59 | 5.16 | 4.86 |

$a/b=0.5$, $b/b_b=5$, $b=1$ m
$N_{xx_{CR}}$ unit is $[N/m]$.

**Table 4**
Convergence and verification with FE analysis, curved panel, linear buckling.

| | $\delta/a$ | 0.000 | 0.200 | 0.400 | 0.600 | 0.807 | 0.907 |
|---|---|---|---|---|---|---|---|
| $m=n=5$ | $N_{xx_{CR}}$ | 33.61 | 33.59 | 33.18 | 32.63 | 32.51 | 32.84 |
| | Error | 4.96% | 5.13% | 4.63% | 4.44% | 7.05% | 10.27% |
| $m=n=6$ | $N_{xx_{CR}}$ | 32.69 | 32.65 | 32.35 | 31.74 | 30.88 | 30.37 |
| | Error | 2.08% | 2.18% | 2.04% | 1.60% | 1.68% | 1.99% |
| $m=n=8$ | $N_{xx_{CR}}$ | 31.93 | 31.88 | 31.62 | 31.12 | 30.28 | 29.68 |
| | Error | −0.27% | −0.22% | −0.27% | −0.38% | −0.30% | -0.35% |
| $m=n=10$ | $N_{xx_{CR}}$ | 31.92 | 31.86 | 31.59 | 31.10 | 30.26 | 29.65 |
| | Error | −0.31% | −0.28% | −0.36% | −0.47% | −0.36% | −0.43% |
| FE | $N_{xx_{CR}}$ | 32.02 | 31.95 | 31.71 | 31.24 | 30.37 | 29.78 |

$a/b=0.5$, $b/b_b=5$, $b=1$ m, $r=10$ m.
$N_{xx_{CR}}$ unit is $[N/m]$.

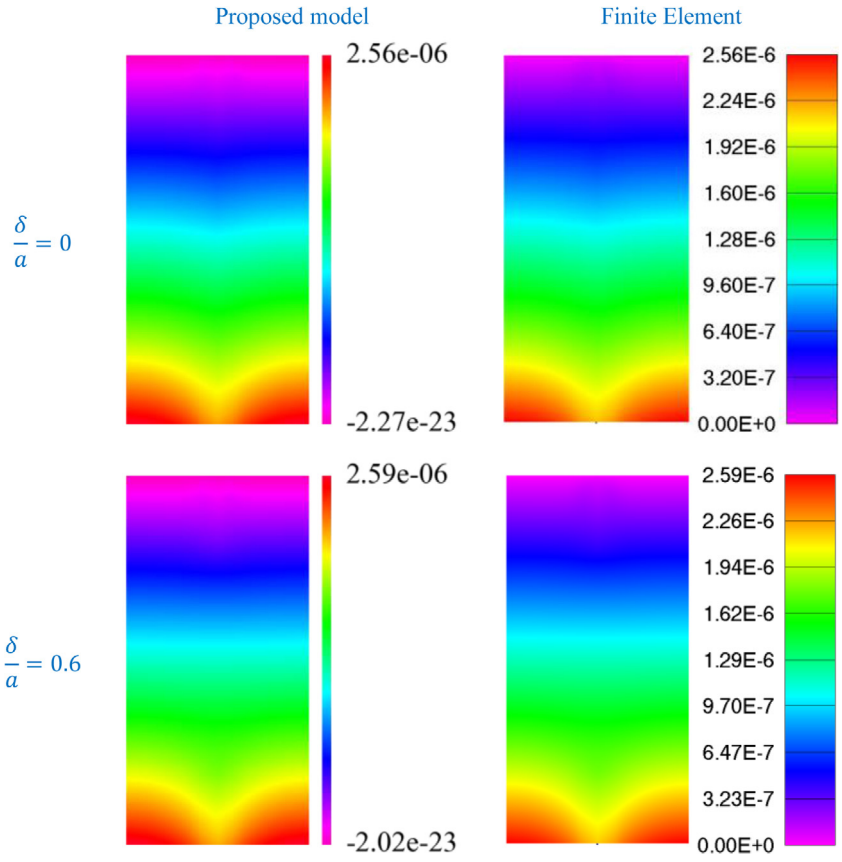


**Fig. 10.** Pre-buckling displacement field $u$ for the skin $[m]$.

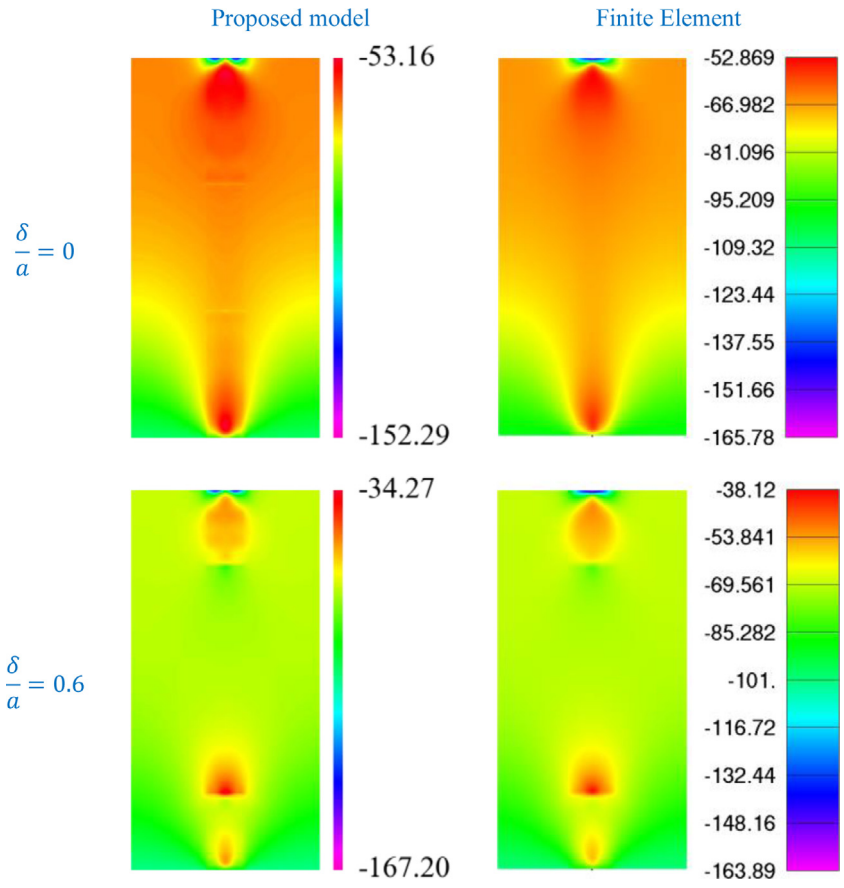


**Fig. 11.** Pre-buckling stress field $N_{xx}$ for the skin $[N/m]$.

obtained from finite element simulations, shown in Fig. 14. A close correlation can be observed, even for the non-symmetric mode obtained with $\delta/a = 0.9$.

### 7.3. Natural frequency with different defect lengths

Natural frequency analyses were performed solving Eq. (28) and using the boundary conditions shown in Fig. 8. Table 5 shows a convergence study and verification against FE results, where the error is relative to the FE model. Stiffened panel #1of Table 2 with $r = 10$ m was used in these comparisons, with $a/b = 0.5$ and $b/b_b = 5$. Similarly to the convergence study performed for linear buckling, errors below 1% start to occur with $m = n = 8$ and this is the chosen refinement applied for all natural frequency runs, unless otherwise specified.

The sensitivity of the natural frequency behavior to various debonding defect lengths was studied for stiffened panel #1 of Table 2, and the results as shown in Fig. 15, where $\omega_{CR}^{\delta=0}$ is the natural frequency with no debonding defect. Results for the other stiffened panel laminate configurations of Table 2 are shown in Appendix C. Interestingly, the impact of the debonding defect length on the natural frequency behavior is very similar to the impact on the linear buckling response already discussed, i.e. the threshold of debonding defect that drastically reduces the first natural frequency is inversely proportional with $a/b$. Again, $b/b_b$ showed to have a minor influence on the natural frequency sensitivity to $\delta/a$.

Natural frequency modes for various $a/b$ ratios and debonding defect sizes are presented in Fig. 16 for $b/b_b = 5$, showing that the abrupt decrease on the first frequency value is due to a change on the critical skin vibration mode. Higher $a/b$ ratios will allow this change to occur for lower $\delta/a$ thresholds, similarly to what was observed for linear buckling modes.

Fig. 17 shows analysis results for stiffened panel #1 of Table 2 with $r = 10$ m, where the natural frequency sensitivity is clearly less dependent on $a/b$ than for flat panels with similar laminates and geometry (cf. Fig. 15). Another important distinction is that for curved panels the $b/b_b$ drastically influences the threshold of $\delta/a$ that will cause abrupt changes on the vibration frequencies.

Critical modes for various configurations of curved panels with $b/b_b$ are presented in Fig. 18 with an eigenvector scale ranging from blue (most negative) to red (most positive), where it becomes apparent that for higher $\delta/a$ and $a/b$ ratios the dominant mode no longer belongs to the skin. In fact, it was observed for these cases that the critical mode belongs to the stiffener's base, which has a free edge at the defect region. For the case with the largest skin-to-stiffener ratio, i.e. $b/b_b = 10$, it was observed that the skin mode remains dominant even for configurations with high $\delta/a$ and high $a/b$; and that is why these configurations are considerably less sensitive to $\delta/a$ than the flat panel counterparts, as observed comparing Figs. 15 and 17 for $b/b_b = 10$.

## 8. Conclusions

The proposed strategy to assemble semi-analytical models showed to be successful to predict the linear buckling and natural vibration behavior of stiffened panels. For the examples herein studies an absolute difference of less than 1% when compared to a finite element model was observed for approximation functions with $m = n = 8$ terms. Conventional single-domain models showed not to allow the prediction of complex and discontinuous

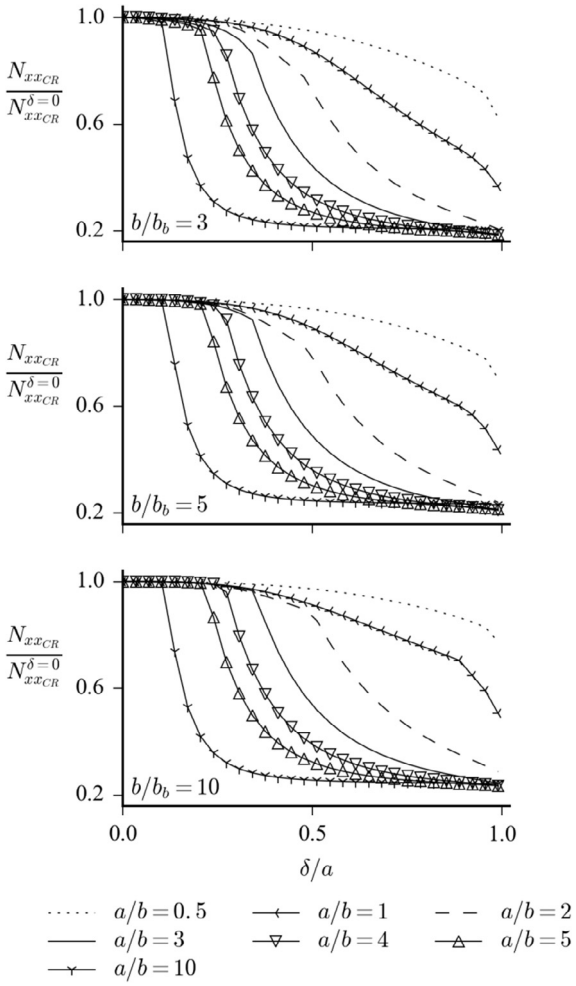


**Fig. 12.** Effect of defect on linear buckling of T-stiffened flat panels.

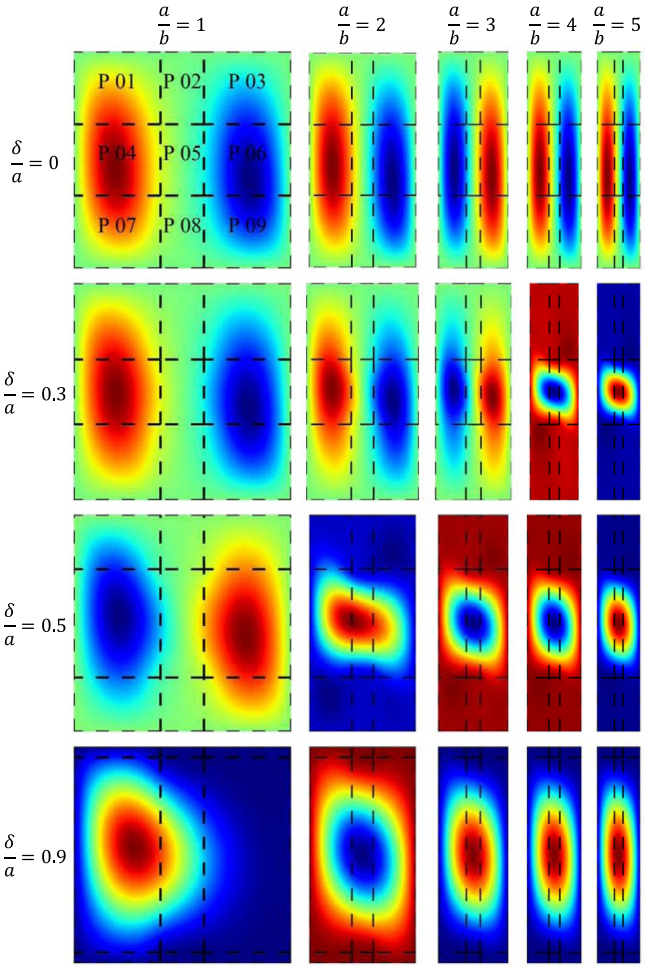


**Fig. 13.** Linear buckling eigenvectors, with $b/b_b = 5$.

displacement fields, which are created when debonding defects are present. The strategy proposed to calculate the penalty stiffnesses based on laminate properties of the adjacent panels showed to result in numerically stable analyses, in contrast to adopt an arbitrarily fixed high value.

Regarding the computational efficiency, it was observed that the stiffness matrices generated for the assembly approach are much sparser compared to single domain models, leading to a considerable reduction of the solving time. The converged finite element herein adopted for the comparisons spent about 12.8 s per linear buckling run, while the proposed model with $m = n = 8$ spent about 3.9 s per run. It is noteworthy to say that for the assembly model the number of terms can be easily reduced if higher performances are required, especially aiming optimization tasks involving huge design spaces. Thus, using for each domain $m = n = 6$ would reduce the run time to 1.2 s, and using $m = n = 5$ to only 0.7 s per run.

The main limitation that one may encounter when applying assembled models are related to the unavailability to find a semi-analytical models for a given domain, e.g. curved cutouts would require special integration schemes not yet implemented [37], and the programming complexity that one may encounter when assembling already existing domains.

The studies carried out with the developed models showed that for debonding defect sizes in the range of $\delta/a \leqslant 0.1$ both flat and curved T-stiffened panels have skin-dominant modes, for both linear buckling and natural frequency.

The vibration analysis of curved panels showed that larger defects in the range $\delta/a > 0.1$ will result in critical modes at the stiffener's base. This is due to the new free edge with the length

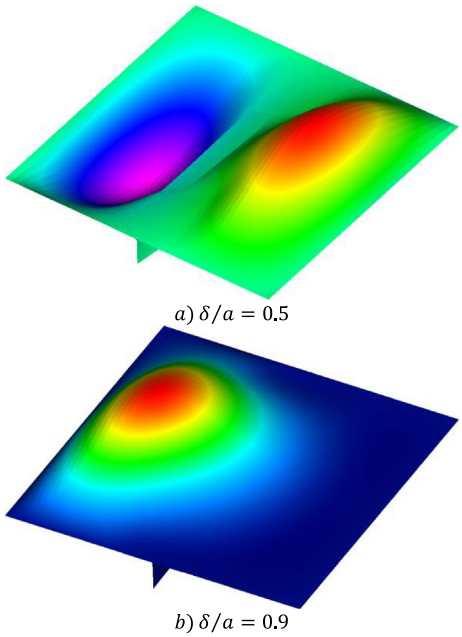


**Fig. 14.** Finite element eigenvectors for laminates #1, with $a/b = 1$ and $b/b_b = 5$.

**Table 5**
Convergence and verification with FE analysis, curved panel, natural frequency.

| | $\delta/a$ | 0.00 | 0.207 | 0.407 | 0.607 | 0.807 | 0.907 |
|---|---|---|---|---|---|---|---|
| $m=n=5$ | $\omega_{CR}$ | 69.81 | 69.67 | 68.56 | 65.45 | 60.59 | 57.77 |
| | Error | 7.86% | 7.97% | 7.96% | 7.09% | 5.39% | 4.01% |
| $m=n=6$ | $\omega_{CR}$ | 65.85 | 65.68 | 64.69 | 62.23 | 58.39 | 56.14 |
| | Error | 1.74% | 1.79% | 1.87% | 1.83% | 1.57% | 1.08% |
| $m=n=8$ | $\omega_{CR}$ | 65.17 | 64.98 | 63.99 | 61.59 | 57.83 | 55.69 |
| | Error | 0.69% | 0.71% | 0.76% | 0.78% | 0.60% | 0.28% |
| $m=n=10$ | $\omega_{CR}$ | 65.13 | 64.93 | 63.92 | 61.52 | 57.77 | 55.62 |
| | Error | 0.63% | 0.62% | 0.66% | 0.66% | 0.48% | 0.15% |
| FE | $\omega_{CR}$ | 64.72 | 64.52 | 63.50 | 61.12 | 57.49 | 55.54 |

$a/b=0.5$, $b/b_b=5$, $b=1$ m.
$\omega_{CR}$ unit is $(Hz)$.

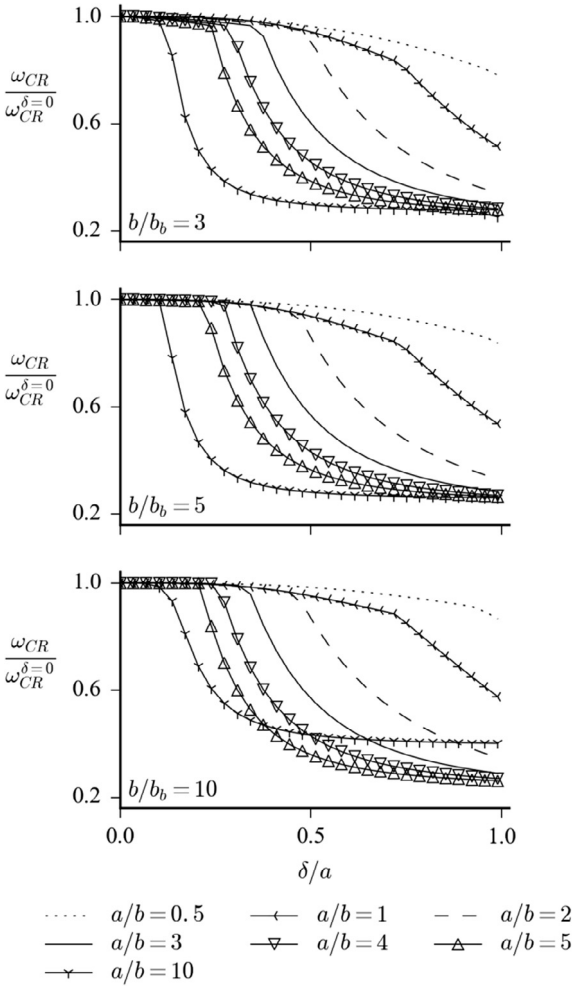


**Fig. 15.** Effect of defect on natural frequency of T-stiffened flat panels.

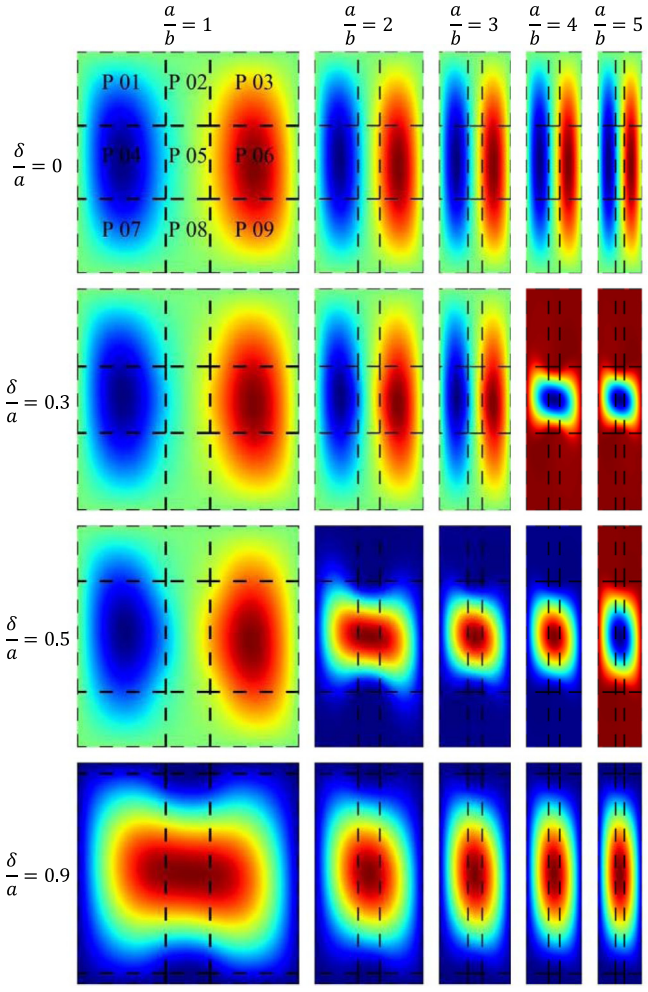


**Fig. 16.** Natural frequency modes, with $b/b_b=5$ for a flat panel.

of the debonding defect. Panels with high skin-to-stiffener ratio tend to be more skin-dominant in the critical mode, showing considerably less sensitivity to the defect size when compared to panels with lower skin-to-stiffener ratio.

Flat panels do not have the curvature stiffening effect acting on the skin such that in all cases herein investigated the dominant mode belongs to the skin, for either linear buckling or natural frequency analysis. A very characteristic mechanism of mode change with increasing defect size has been observed, which is characterized by a shift between one semi-wave at each side of the T-stiffener to a single buckle centered at the debonding defect region. When the mode shifts to a single buckle there is an abrupt change of either the critical linear buckling load or the first natural frequency, leading to a critical $\delta/a$ defect size value. This threshold decreases with the increase of $a/b$ ratio.

As an ultimate conclusion, it was observed that debonding defects up to $\delta/a=0.1$ do not significantly affect the critical linear buckling load neither the first natural frequency of T-stiffened flat panels or curved panels. However, further studies are recommended to extend the current investigation in order to obtain a more thorough guideline:

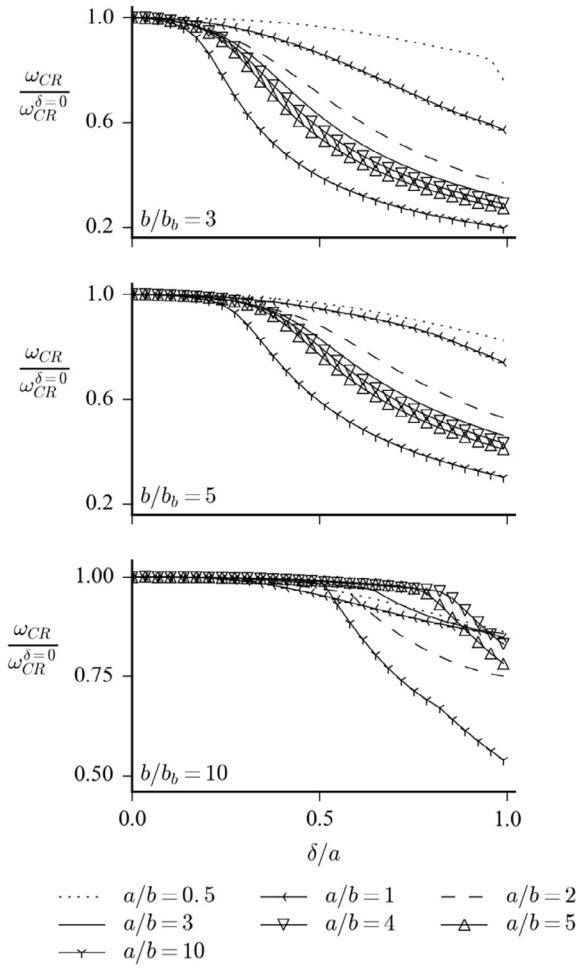


**Fig. 17.** Effect of defect on natural frequency of T-stiffened curved panels.

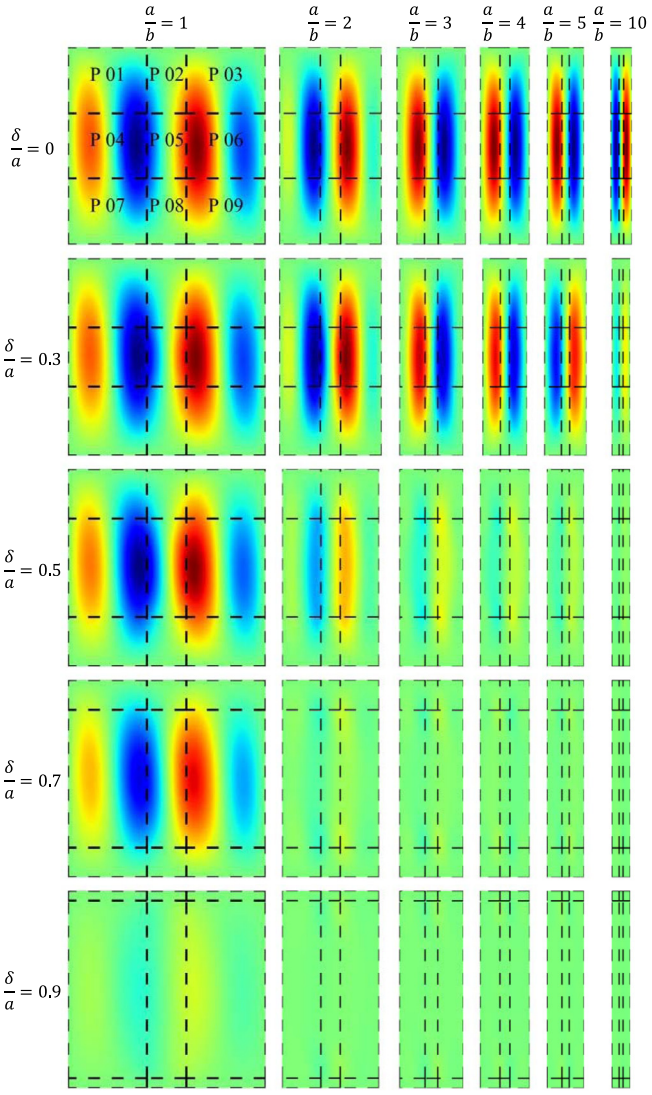


**Fig. 18.** Natural frequency modes, with $b/b_b = 5$ for a cylindrical panel with $r = 10$ m.

- linear buckling and natural frequency sensitivity to a debonding defect for loads perpendicular to the stiffener axis ($N_{yy}$) and combined load cases;
- configurations with various radius-to-thickness ratios in order to verify if a threshold beyond which only skin-dominant modes exist (such as it was observed for the flat panels herein addressed);
- different $b_f/b_b$ ratios for T-stiffened panels;
- different stiffener profiles;
- non-linear analysis considering stress concentrations at the region near the debonding defect in order to achieve more realistic simulation scenarios.

Additional studies could also extend the present model to simulate riveted stiffened panels in order to address the effect of defects produced by losing one or more rivets in the residual strength. Further studies are also encouraged applying the modelling technique herein addressed to structures with cutouts, for which the displacement field has discontinuities and therefore single-domain models would not be easily applicable. The semi-analytical models herein proposed are made available in the CompMech scientific package [37]

## Acknowledgments

To the free software communities that have provided convenient packages for the Python programming language: the Matplotlib [38] community with a complete plotting library; the Cython community with a very straightforward package that links the performance of the C programming language with the flexibility of Python [39]; the SciPy and NumPy communities that have provided Python modules for scientific and numeric analysis [40]; the SymPy [41] community that has provided Python modules for symbolic manipulation. The authors are also grateful to the Brazilian Research Council – CNPq for the continued support to their research work, especially through research project number 300990/2013-8.

## Appendix A. Constitutive stiffenesses for laminae

The local stiffness terms [25] of the laminae engineering constants for the $k^{th}$ layer are:

$$\begin{aligned} Q_{11} &= \frac{E_1}{1-\nu_{12}\nu_{21}}, \quad Q_{12} = \frac{\nu_{12}E_2}{1-\nu_{12}\nu_{21}} \\ Q_{22} &= \frac{E_2}{1-\nu_{12}\nu_{21}}, \quad Q_{66} = G_{12} \end{aligned} \tag{A.1}$$

The global stiffness terms for the $k^{th}$ layer in respect to the laminate coordinates system is given as follows [25]:

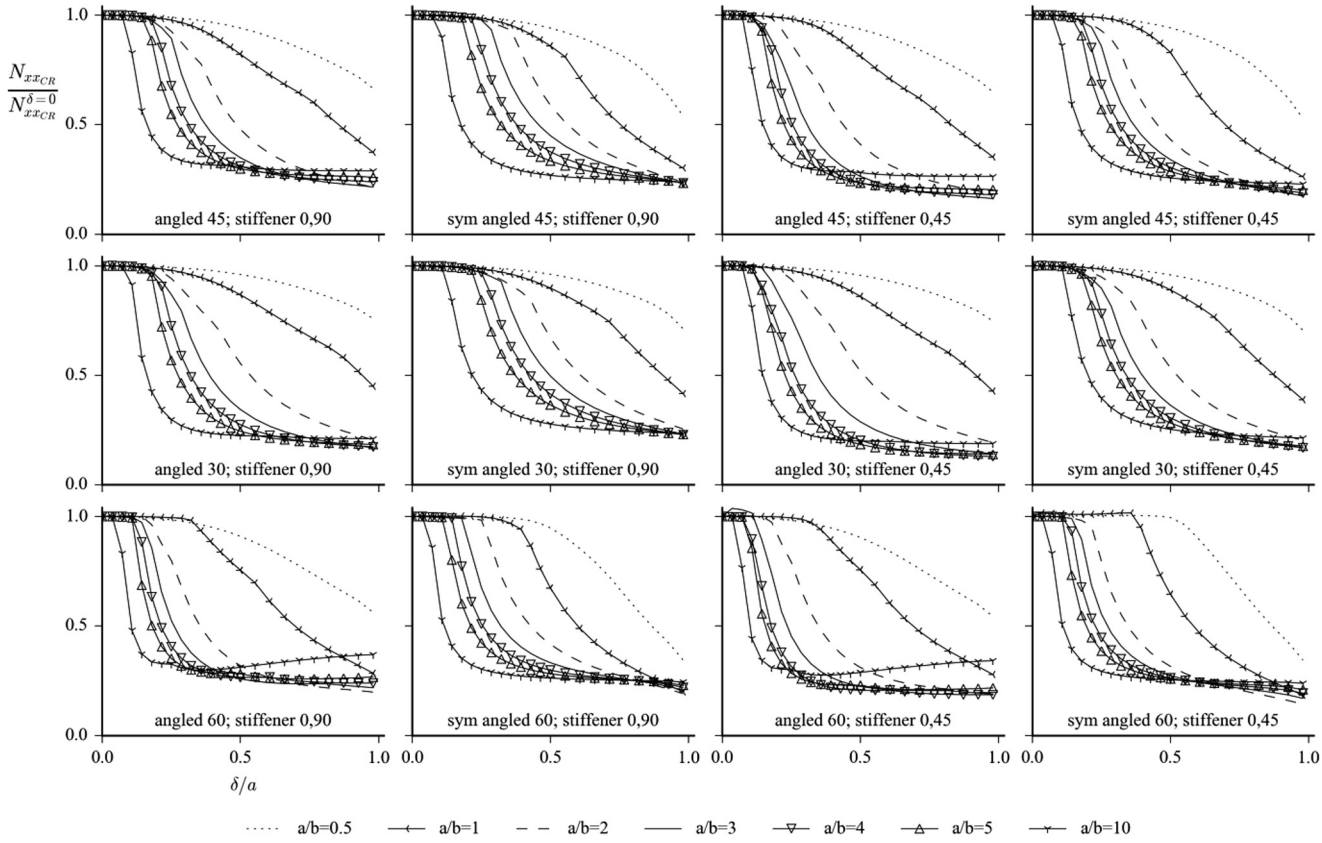


**Fig. C.1.** Linear buckling, T-stiffened flat panels with $b/b_b = 5$.

$$
\begin{aligned}
\bar{Q}_{11} &= Q_{11}\cos^4\theta + 2(Q_{12}+2Q_{66})\sin^2\theta\cos^2\theta + Q_{22}\sin^4\theta \\
\bar{Q}_{12} &= (Q_{11}+Q_{22}-4Q_{66})\sin^2\theta\cos^2\theta + Q_{12}(\sin^4\theta+\cos^4\theta) \\
\bar{Q}_{22} &= Q_{11}\sin^4\theta + 2(Q_{12}+2Q_{66})\sin^2\theta\cos^2\theta + Q_{22}\cos^4\theta \\
\bar{Q}_{16} &= (Q_{11}-Q_{12}-2Q_{66})\sin\theta\cos^3\theta + (Q_{12}-Q_{22}+2Q_{66})\sin^3\theta\cos\theta \\
\bar{Q}_{26} &= (Q_{11}-Q_{12}-2Q_{66})\sin^3\theta\cos\theta + (Q_{12}-Q_{22}+2Q_{66})\sin\theta\cos^3\theta \\
\bar{Q}_{66} &= (Q_{11}+Q_{22}-2Q_{12}-2Q_{66})\sin^2\theta\cos^2\theta + Q_{66}(\sin^4\theta+\cos^4\theta)
\end{aligned}
\tag{A.2}
$$

## Appendix B. Expressions for structural matrices

In the equations below $u$, $v$ and $w$ are in fact abbreviations for $S^u$, $S^v$ and $S^w$, for the sake of clarity.

Since three degrees of freedom exist each minimum repeatable term of each panel matrix ($\boldsymbol{K}$, $\boldsymbol{K_p}$ and $\boldsymbol{M_p}$) will consist of a $3 \times 3$ square matrix, located row-wise by indices $i,j$ and column-wise by indices $k,\ell$. Therefore, only the calculation of this minimum repeatable term has to be given.

Constitutive stiffness matrix $\boldsymbol{K_p}$:

$$
\begin{aligned}
K_p^{ijkl}(1,1) &= A_{11}\tfrac{b}{a}u_{,\xi}^{ij}u_{,\xi}^{k\ell} + A_{16}\left(u_{,\xi}^{ij}u_{,\eta}^{k\ell} + u_{,\eta}^{ij}u_{,\xi}^{k\ell}\right) + A_{66}\tfrac{a}{b}\left(u_{,\eta}^{ij}u_{,\eta}^{k\ell}\right) \\
K_p^{ijkl}(1,2) &= A_{12}u_{,\xi}^{ij}v_{,\eta}^{k\ell} + A_{16}\tfrac{b}{a}\left(u_{,\xi}^{ij}v_{,\xi}^{k\ell}\right) + A_{26}\tfrac{a}{b}\left(u_{,\eta}^{ij}v_{,\eta}^{k\ell}\right) + A_{66}u_{,\eta}^{ij}v_{,\xi}^{k\ell} \\
K_p^{ijkl}(1,3) &= -2\tfrac{b}{a^2}B_{11}\left(u_{,\xi}^{ij}w_{,\xi\xi}^{k\ell}\right) - \tfrac{2}{b}B_{12}\left(u_{,\xi}^{ij}w_{,\eta\eta}^{k\ell}\right) - \tfrac{2}{a}B_{16}\left(2u_{,\xi}^{ij}w_{,\xi\eta}^{k\ell} + u_{,\eta}^{ij}w_{,\xi\xi}^{k\ell}\right) - 2\tfrac{a}{b^2}B_{26}\left(u_{,\eta}^{ij}w_{,\eta\eta}^{k\ell}\right) - \tfrac{4}{b}B_{66}\left(u_{,\eta}^{ij}w_{,\xi\eta}^{k\ell}\right) + \delta_{panel}\tfrac{1}{2r}\left(bA_{12}u_{,\xi}^{ij}w^{k\ell} + aA_{26}u_{,\eta}^{ij}w^{k\ell}\right) \\
K_p^{ijkl}(2,1) &= A_{12}v_{,\eta}^{ij}u_{,\xi}^{k\ell} + A_{16}\tfrac{b}{a}v_{,\xi}^{ij}u_{,\xi}^{k\ell} + A_{26}\tfrac{a}{b}v_{,\eta}^{ij}u_{,\eta}^{k\ell} + A_{66}v_{,\xi}^{ij}u_{,\eta}^{k\ell} \\
K_p^{ijkl}(2,2) &= A_{22}\tfrac{a}{b}v_{,\eta}^{ij}v_{,\eta}^{k\ell} + A_{26}\left(v_{,\xi}^{ij}v_{,\eta}^{k\ell} + v_{,\eta}^{ij}v_{,\xi}^{k\ell}\right) + A_{66}\tfrac{b}{a}v_{,\xi}^{ij}v_{,\xi}^{k\ell} \\
K_p^{ijkl}(2,3) &= -\tfrac{2}{a}B_{12}v_{,\eta}^{ij}w_{,\xi\xi}^{k\ell} - 2\tfrac{b}{a^2}B_{16}v_{,\xi}^{ij}w_{,\xi\xi}^{k\ell} - 2\tfrac{a}{b^2}B_{22}v_{,\eta}^{ij}w_{,\eta\eta}^{k\ell} - \tfrac{2}{b}B_{26}\left(v_{,\xi}^{ij}w_{,\eta\eta}^{k\ell} + 2v_{,\eta}^{ij}w_{,\xi\eta}^{k\ell}\right) - \tfrac{4}{a}B_{66}v_{,\xi}^{ij}w_{,\xi\eta}^{k\ell} + \delta_{panel}\left(\tfrac{a}{2r}A_{22}v_{,\eta}^{ij}w^{k\ell} + \tfrac{b}{2r}A_{26}v_{,\xi}^{ij}w^{k\ell}\right) \\
K_p^{ijkl}(3,1) &= -2\tfrac{b}{a^2}B_{11}w_{,\xi\xi}^{ij}u_{,\xi}^{k\ell} - \tfrac{2}{b}B_{12}w_{,\eta\eta}^{ij}u_{,\xi}^{k\ell} - 2\tfrac{a}{b^2}B_{26}w_{,\eta\eta}^{ij}u_{,\eta}^{k\ell} - \tfrac{4}{b}B_{66}w_{,\xi\eta}^{ij}u_{,\eta}^{k\ell} - \tfrac{2}{a}B_{16}\left(2w_{,\xi\eta}^{ij}u_{,\xi}^{k\ell} + w_{,\xi\xi}^{ij}u_{,\eta}^{k\ell}\right) + \delta_{panel}\left(\tfrac{a}{2r}A_{26}w^{ij}u_{,\eta}^{k\ell} + \tfrac{b}{2r}A_{12}w^{ij}u_{,\xi}^{k\ell}\right) \\
K_p^{ijkl}(3,2) &= -\tfrac{2}{a}B_{12}w_{,\xi\xi}^{ij}v_{,\eta}^{k\ell} - 2\tfrac{a}{b^2}B_{22}w_{,\eta\eta}^{ij}v_{,\eta}^{k\ell} - \tfrac{4}{a}B_{66}w_{,\xi\eta}^{ij}v_{,\xi}^{k\ell} - \tfrac{2}{b}B_{26}\left(w_{,\eta\eta}^{ij}v_{,\xi}^{k\ell} + 2w_{,\xi\eta}^{ij}v_{,\eta}^{k\ell}\right) - 2\tfrac{b}{a^2}B_{16}w_{,\xi\xi}^{ij}v_{,\xi}^{k\ell} + \delta_{panel}\left(\tfrac{a}{2r}A_{22}w^{ij}v_{,\eta}^{k\ell} + \tfrac{b}{2r}A_{26}w^{ij}v_{,\xi}^{k\ell}\right) \\
K_p^{ijkl}(3,3) &= 4\tfrac{b}{a^3}D_{11}w_{,\xi\xi}^{ij}w_{,\xi\xi}^{k\ell} + \tfrac{4}{ab}D_{12}\left(w_{,\xi\xi}^{ij}w_{,\eta\eta}^{k\ell} + w_{,\eta\eta}^{ij}w_{,\xi\xi}^{k\ell}\right) + 4\tfrac{a}{b^3}D_{22}w_{,\eta\eta}^{ij}w_{,\eta\eta}^{k\ell} + \tfrac{8}{a^2}D_{16}\left(w_{,\xi\xi}^{ij}w_{,\xi\eta}^{k\ell} + w_{,\xi\eta}^{ij}w_{,\xi\xi}^{k\ell}\right) + \tfrac{8}{b^2}D_{26}\left(w_{,\xi\eta}^{ij}w_{,\eta\eta}^{k\ell} + w_{,\eta\eta}^{ij}w_{,\xi\eta}^{k\ell}\right) \\
&\quad + \tfrac{16}{ab}D_{66}w_{,\xi\eta}^{ij}w_{,\xi\eta}^{k\ell} - \delta_{panel}\tfrac{b}{ar}B_{12}\left(w_{,\xi\xi}^{ij}w^{k\ell} + w^{ij}w_{,\xi\xi}^{k\ell}\right) - \delta_{panel}\tfrac{a}{br}B_{22}\left(w_{,\eta\eta}^{ij}w^{k\ell} + w^{ij}w_{,\eta\eta}^{k\ell}\right) - \delta_{panel}\tfrac{2}{r}B_{26}\left(w_{,\xi\eta}^{ij}w^{k\ell} + w^{ij}w_{,\xi\eta}^{k\ell}\right) + \delta_{panel}^2\tfrac{ab}{4r^2}A_{22}w^{ij}w^{k\ell}
\end{aligned}
\tag{B.1}
$$

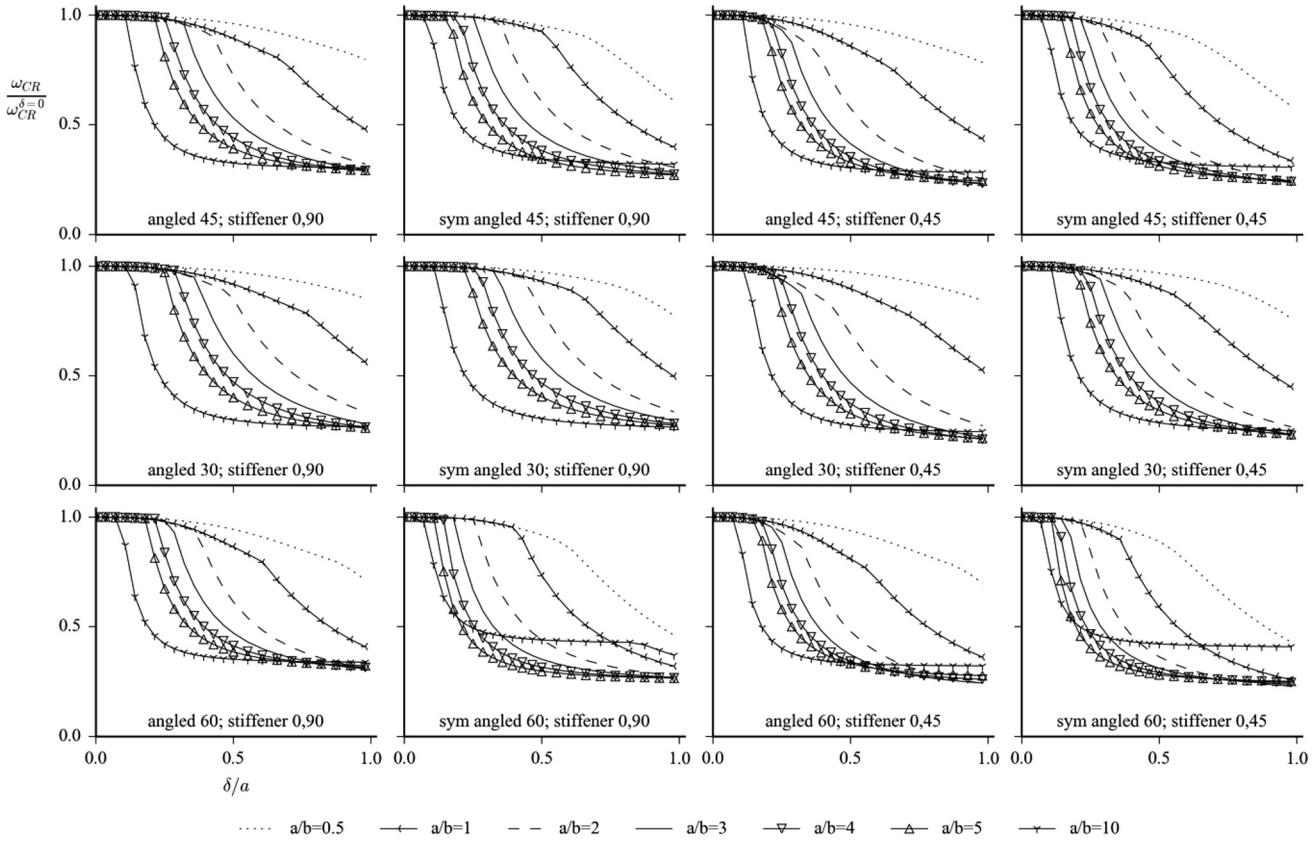


**Fig. C.2.** Natural frequency, T-stiffened flat panels with $b/b_b = 5$.

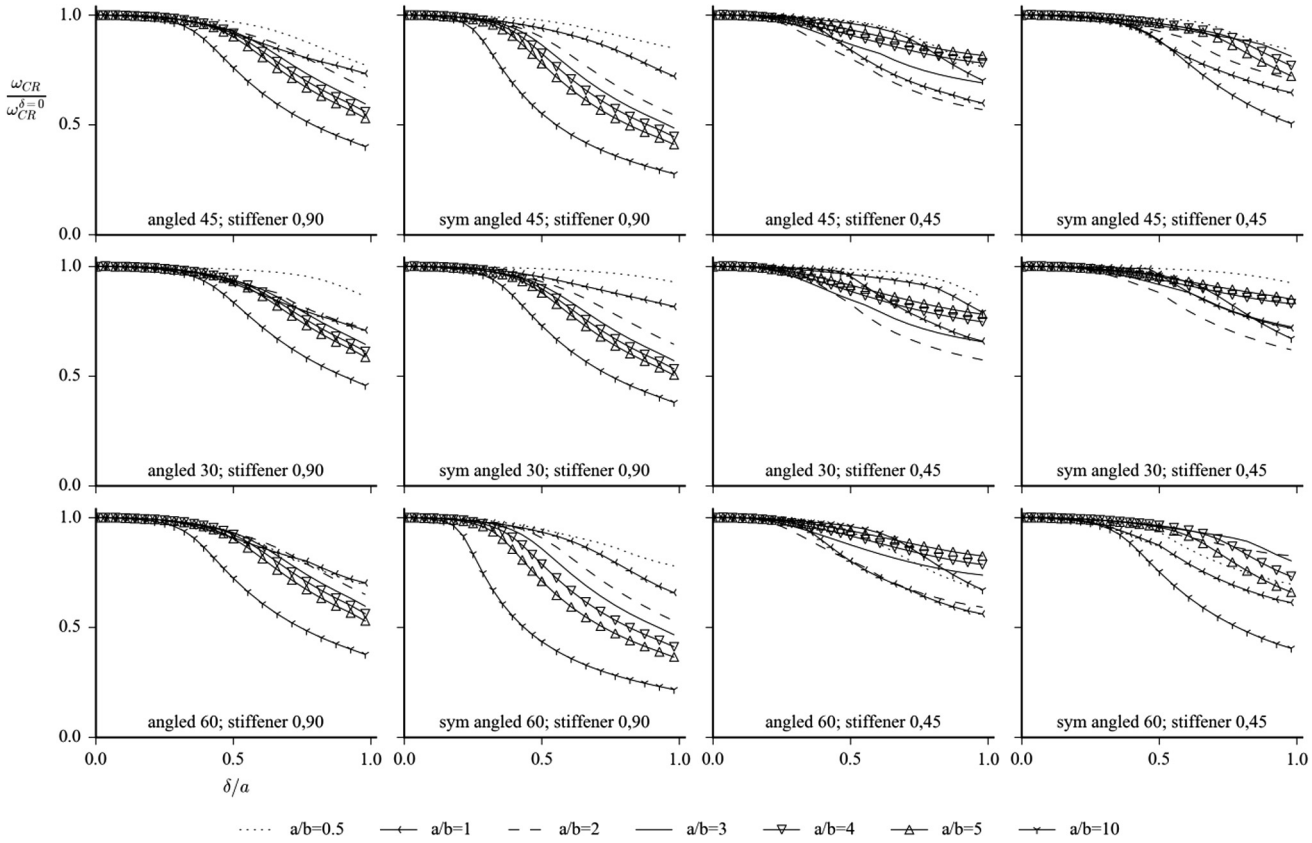


**Fig. C.3.** Natural frequency, T-stiffened curved panel with $b/b_b = 5$ and $r = 10$ m.

Initial stress (or geometric) stiffness matrix $\boldsymbol{K}_{G_p}$:

$$K^{ijkl}_{G_p}(3,3) = N_{xx} w^{ij}_{\xi} w^{k\ell}_{\xi} \frac{b}{a} + N_{yy} w^{ij}_{\eta} w^{k\ell}_{\eta} \frac{a}{b} + N_{xy}(w^{ij}_{\eta} w^{k\ell}_{\xi} + w^{ij}_{\xi} w^{k\ell}_{\eta}) \quad \text{(B.2)}$$

with $N_{xx}$, $N_{yy}$ and $N_{xy}$ calculated using Eq. (14)

Mass matrix $\boldsymbol{M_p}$:

$$\begin{aligned} M^{ijkl}_{p}(1,1) &= \tfrac{ab}{4} h\ \mu\ u^{ij} u^{k\ell} \\ M^{ijkl}_{p}(2,2) &= \tfrac{ab}{4} h\ \mu\ v^{ij} v^{k\ell} \\ M^{ijkl}_{p}(3,3) &= \tfrac{ab}{4} h\ \mu \left( w^{ij} w^{k\ell} + \tfrac{1}{3} w^{ij}_{\xi} w^{k\ell}_{\xi} \left(\tfrac{h}{a}\right)^2 + \tfrac{1}{3} w^{ij}_{\eta} w^{k\ell}_{\eta} \left(\tfrac{h}{b}\right)^2 \right) \end{aligned} \quad \text{(B.3)}$$

## Appendix C. Results for configurations of Table 2

See Figs. C.1–C.3

## References


[1] Niu MCY. Airframe structural design: practical design information and data on aircraft structures. New York: Wiley; 1998.
[2] Fisher JW, Struik JHA. Guide to design criteria for bolted and riveted joints. New York: Wiley; 1974.
[3] Bickford JH. The bolting technology council and the search for more accurate preload. ASME Pressure Vessels and Piping Conference on Advances in Bolted Joint Technology 1989;vol. 158:1–6.
[4] Bickford JH. An introduction to the design and behavior of bolted joints. 2nd ed. New York: Marcel Dekker Inc.; 1990.
[5] Fernlund G, Papini M, McCammond D, Spelt JK. Fracture load predictions for adhesive joints. Compos Sci Technol 1994;51:587–600.
[6] Bisagni C. Progressive delamination analysis of stiffened composite panels in post-buckling. In: Proceedings of the 47 AIAA/ASME/ASCE;AHS/ASC Structures, Structural Dynamics and Materials Conference, Rhode Island; 2006.
[7] Orifici AC, Alberdi IOZ, Thomson RS, Bayandor J. Compression and post-buckling damage growth and collapse analysis of flat composite stiffened panels. Compos Sci Technol 2008;68:3150–60.
[8] Balzani C, Wagner W. Numerical treatment of damage propagation in axially compressed composite airframe panels. Int J Struct Stab Dyn 2010;10 (4):683–703.
[9] Ambur DR, Jaunky N, Hilburger MW. Progressive failure studies of stiffened panels subjected to shear loading. Compos Struct 2004;65:129–42.
[10] Rijn JCFNV, Wiggenraad JFM. A seven-point bending test to determine the strength of the skin stiffener interface in composite aircraft panels. National Aerospace Laboratory NLR (NLR-TP-2000-044); 2000.
[11] Mittelstedt C. Closed-form buckling analysis of stiffened composite plates and identification of minimum stiffener requirements. Int J Eng Sci 2008;46:1011–34.
[12] Mittelstedt C, Beerhorst M. Closed-form buckling analysis of compressively loaded composite plates braced by omega-stringers. Compos Struct 2009;88:424–35.
[13] Bisagni C, Vescovini R. Analytical formulation for local buckling and post-buckling analysis of stiffened laminated panels. Thin-Walled Struct 2009;47:318–34.
[14] Stamatelos DG, Labeas GN, Tserpes KI. Analytical calculation of local buckling and post-buckling behavior of isotropic and orthotropic stiffened panels. Thin-Walled Struct 2011;49:422–30.
[15] Mittelstedt C. Explicit local buckling analysis of stiffened composite plates accounting for periodic boundary conditions and stiffener-plate interaction. Compos Struct 2009;91:249–65.
[16] Mittelstedt C, Schröder K-U. Local postbuckling of hat-stringer-stiffened composite laminated plates under transverse compression. Compos Struct 2010;92:2830–44.
[17] Vescovini R, Bisagni C. Semi-analytical buckling analysis of omega stiffened panels under multi-axial loads. Compos Struct 2015;120:285–99.
[18] Frocht MM, Hill HN. Stress-concentration factors around a central circular hole in a plate loaded through a pin in the hole. ASME J Appl Mech 1940;7:A4–9.
[19] Dohner, JL. White paper: on the development of methodologies for constructing predictive models of structures with joints and interfaces. Sandia National Laboratories SAND2001-0003P; 2001.
[20] Rikards R, Chate A, Ozolinsh O. Analysis for buckling and vibrations of composite stiffened shells and plates. Compos Struct 2001;51:361–70.
[21] Ibrahim RA. Structural dynamics with parameter uncertainties. ASME Appl Mech Rev 1987;40:309–28.
[22] Ibrahim RA, Pettit CL. Uncertainties and dynamic problems of bolted joints and other fasteners. J Sound Vib 2005;279:857–936.
[23] Agarwal BD, Broutman LJ. Analysis and performance of fiber composites. New York: Wiley; 1990.
[24] Loughlan J. The buckling performance of composite stiffened panel structures subjected to combined in-plane compression and shear loading. Compos Struct 1994;29:197–212.
[25] Reddy JN. Mechanics of laminated composite plates and shells, theory and analysis. 2nd ed. Boca Raton: CRC Press; 2004.
[26] Donnell LH. A new theory for the buckling of thin cylinders under axial compression and bending. ASME Trans 1934;56:795–806.
[27] Castro SGP, Mittelstedt C, Monteiro FAC, Arbelo MA, Degenhardt R. A semi-analytical approach for the linear and non-linear buckling analysis of imperfect unstiffened laminated composite cylinders and cones under axial, torsion and pressure loads. Thin-Walled Struct 2015;90(May):61–73.
[28] Ferreira AJM, Barbosa JT. Buckling behaviour of composite shells. Compos Struct 2000;50(1):93–8.
[29] Castro SGP, Mittelstedt C, Monteiro FAC, Arbelo MA, Ziegmann G, Degenhardt R. Linear buckling predictions of unstiffened laminated composite cylinders and cones under various loading and boundary conditions using semi-analytical models. Compos Struct 2014;118:303–15.
[30] Abbott P. Tricks of the trade: Legendre-Gauss quadrature. Math J 2005;9:689–91.
[31] Castro SGP, Guimarães TAM, Rade DA, Donadon MV. Flutter of stiffened composite panels considering the stiffener's base as a structural element. Compos Struct 2016;140:36–43.
[32] Peano AG. Hierarchies of conforming finite elements for plate elasticity and plate bending. Comput Math Appl 1976;2:211–24.
[33] Zhu DC. Development of hierarchical finite element methods at BIA. In: Proceedings of the International Conference on Computational Mechanics, May 1985, Tokyo; 1986.
[34] Bardell NS. Free vibration analysis of a flat plate using the hierarchical finite element method. J Sound Vib 1991;151(2):263–89.
[35] Bardell NS, Dunsdon JM, Langley RS. Free and forced vibration analysis of thin, laminated, cylindrically curved panels. Compos Struct 1997;38(1–4):453–62.
[36] Bardell NS, Dunsdon JM, Langley RS. On the free vibration of completely free, open, cylindrically curved, isotropic shell panels. J Sound Vib 1997;207 (5):647–69.
[37] Castro, SGP. Computational Mechanics Tools, Version 0.7.1. 1 November 2016. [Online]. Available: http://compmech.github.io/compmech/.
[38] Hunter JD. Matplotlib: A 2D graphics environment. Comput Sci Eng 2007;9 (3):90–5.
[39] Behnel S, Bradshaw R, Citro C, Dalcin L, Seljebotn DS, Smith K. Cython: the best of both worlds. Comput Sci Eng 2011;13(2):31–9.
[40] Oliphant TE. Python for scientific computing. Comput Sci Eng 2007;9 (3):10–20.
[41] SymPy Development Team. SymPy: Python library for symbolic mathematics; 2013. [Online]. Available: http://www.sympy.org.